Available online at www.sciencedirect.com
SCIENCE DIRECT®
Journal of Computational Physics 209 (2005) 47–81
JOURNAL OF COMPUTATIONAL PHYSICS
www.elsevier.com/locate/jcp

Time-independent finite difference analysis of fully non-linear and viscous fluid sloshing in a rectangular tank

Bang-Fuh Chen [a,b,*], Roger Nokes [b]

[a] Department of Marine Environment and Engineering, National Sun Yat-Sen University, Kaohsiung 804, Taiwan
[b] Department of Civil Engineering, University of Canterbury, Christchurch, New Zealand

Received 18 June 2004; received in revised form 10 February 2005; accepted 2 March 2005
Available online 10 May 2005

Abstract

A novel, time-independent finite-difference method for analyzing complete two-dimensional sloshing motion (surge, heave and pitch) in a tank has been developed based on the primitive 2D Navier–Stokes equations. Both the fully non-linear free surface condition and fluid viscosity are included. The boundary of the tank is mapped onto a fixed square domain through proper mapping functions and stretched meshes are employed near boundaries in order to more accurately evaluate the large disturbance of fluid along the boundary.

The sloshing displacement agrees well with previously published results. The maximum transient amplitude is much larger than that of the steady-state. Clear beating phenomenon can be found when the tank is excited by near resonance frequency. The frequency dependence and Reynolds number effects are studied. For a fixed forcing-function amplitude, the sloshing response is greatest near resonance. An analysis under coupled surge and pitch motions is also made. The coupling effect is significant and simultaneous surge, heave and pitch motions should be included in the tank sloshing analysis. A simple formula is derived to approximate the horizontal force coefficient, C_F, on the tank walls. The formula implies that C_F is dominated by the free surface displacement when the tank is excited by small surge frequencies. Whereas C_F is attributed to added mass effects when the tank is under higher surge frequency forcing. A power spectra analysis is made to analyze the time series of sloshing displacement. For lower frequency of excitation, the system presents two peaks corresponding to the forcing frequency and fundamental frequency of the system. For higher frequency of excitation, the system shows only one major peak at the fundamental frequency. The limitations of the proposed method are also discussed.

Keywords: Fully non-linear analysis; Sloshing viscous fluid; Time-independent finite difference method; Coupled surge pitch and heave motions

* Corresponding author. Fax: +886 7 5255065.
E-mail address: chenbf@mail.nsysu.edu.tw (B.-F. Chen).

0021-9991/$ - see front matter © 2005 Elsevier Inc. All rights reserved.
doi:10.1016/j.jcp.2005.03.006

1. Introduction

Numerous analytical, numerical and experimental analyses of the seismic response of fluid sloshing in a tank have been published during the last two decades. Ibrahim et al. [28] provide a detailed survey of the CFD research and a general insight into sloshing problems, while Cariou and Casella [4] give a review of commercial CFD codes as applied to this problem. The reported CFD methods include some or all of the following: fluid viscosity, non-linear free surface conditions (weakly or fully non-linear) and wall conditions.

The earliest analyses were simply linear, weakly non-linear and inviscid analyses (such as [2,16,19] among many others). In the years following 1990, fully non-linear free surface boundary conditions, complete primitive Navier–Stokes equations and fluid viscosity were included in the published models. Neglecting the convective acceleration, and using both a velocity correction method and a Lagrangian finite element method, Okamoto and Kawahara [29] incorporated the viscosity of fluid in their analysis of the seismic response of a sloshing fluid. However, in their model, the free surface velocity and the hydrodynamic pressure at the free surface, rather than being calculated from the dynamic free surface boundary conditions, were simply given values. By solving the depth-averaged Navier–Stokes equations for shallow water, Koh et al. [14] studied the effects of rectangular liquid dampers on the reduction of structural vibration during earthquakes. The free surface condition and the base shear were approximated empirically.

Armenio and Rocca [1] analyzed the sloshing of water in a rectangular container under pitch-motion excitation. Kim [13] used a SOLA scheme to solve the primitive Navier–Stokes equations, including the free surface boundary condition, and studied the sloshing flow in 2D and 3D liquid containers, with and without internal baffles. The governing flow equations were written in the moving coordinate system of the tank. The tank was covered with a ceiling and the impact load was studied in the analysis. Both reports ignored surface tension and the tangential stresses at the free surface, and assumed a zero hydrodynamic pressure at the free surface. Wu et al. [21] presented an analytical solution of the linearized Navier–Stokes equations with a linear free-surface condition for sloshing free surface waves in a two-dimensional rectangular tank. All the non-linear terms and complete free surface boundary conditions were neglected in the analysis. That study reported the effect of viscous effects and exciting frequencies on the sloshing history for small Reynolds numbers. Celebi and Akyildiz [5] reported a 2D tank viscous sloshing analysis. Again the Navier–Stokes equations were written in the moving coordinate system of the tank which was forced to move harmonically along a vertical curve with rolling motion. The free surface motion was calculated by the volume of fluid (VOF) technique.

Under zero gravity, Billinghen [3] studied the non-linear sloshing of fluid in a two-dimensional tank. A fully non-linear free surface boundary condition and viscous free surface effects were included in the analysis. The velocity of the contact line was a given single-valued function of the dynamic contact angle (surface gradient) between the fluid and the solid wall. Most recently, Hill [11] presented a weakly non-linear analysis of the transient evolution of 2D standing waves in a rectangular tank. Frandsen [10] reported a fully non-linear finite difference model for inviscid sloshing fluid in tanks.

The most publications mentioned above are for a tank excited by a single forcing function (surge or heave). Although, the sloshing phenomena are complex and abundant, these papers provide only limited discussions of the various flow features that arise in problems of this nature. This paper aims to analyze a wider range of sloshing phenomena.

In this study, a time-independent finite difference method is developed to solve the two-dimensional incompressible Navier–Stokes equations with fully non-linear free surface boundary conditions. The governing equations are written in a coordinate system moving with the tank. The difficulties associated with the time varying free surface boundary are overcome by the use of proper mapping functions that transform the computational domain to a fixed unit square. The advantage of the proposed method is that the flow equations are solved in a rectangular grid and boundary tracing is not needed during the solution

process. Furthermore, re-meshing, due to the moving free surface, is avoided and the mapping precludes the need to calculate the free surface velocity components explicitly. In addition, smoothing of the free surface through spatial filtering is unnecessary. However, the disadvantage of the method is that the mapping function is a non-orthogonal single-valued function and the method is not suitable for large excitation displacements. Thus, the range of allowable forcing amplitudes is limited.

Section 2 introduces the equations of motion for a coordinate system fixed to an accelerating tank. The fully non-linear free surface boundary conditions are also discussed. Section 3 describes the coordinate transformations that map the time-dependent domain into a fixed unit square and allow for mesh stretching at the boundaries. A sensible non-dimensionalization of the governing equations is also presented. The proposed finite-difference method is developed in Section 4 where the full iterative procedure is introduced. Finally, Section 5 presents the detailed results and provides some discussion.

2. Equations of motion

A fully non-linear model of viscous 2-D waves in a numerical wave tank was developed. As the coordinate system is chosen to move with the tank motions (including surge, heave and pitch motions, see Fig. 1), the Navier–Stokes equations can be derived and written as ([7,5,27]):

$$\frac{\partial u}{\partial t}+u\frac{\partial u}{\partial x}+w\frac{\partial u}{\partial z}-2\dot{\theta}w=-g\sin\theta-\frac{1}{\rho}\frac{\partial p}{\partial x}+z\ddot{\theta}+x\dot{\theta}^2-\ddot{x}_c+v\left(\frac{\partial^2 u}{\partial x^2}+\frac{\partial^2 u}{\partial z^2}\right), \tag{1}$$

$$\frac{\partial w}{\partial t}+u\frac{\partial w}{\partial x}+w\frac{\partial w}{\partial z}-2\dot{\theta}u=-g\cos\theta-\frac{1}{\rho}\frac{\partial p}{\partial z}-x\ddot{\theta}+z\dot{\theta}^2-\ddot{z}_c+v\left(\frac{\partial^2 w}{\partial x^2}+\frac{\partial^2 w}{\partial z^2}\right). \tag{2}$$

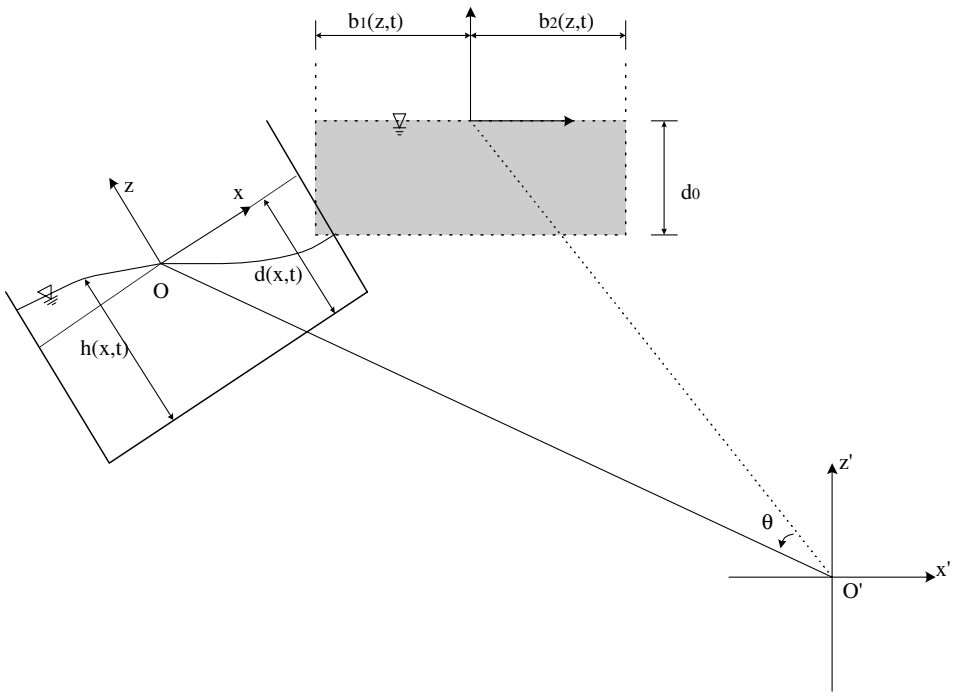

Fig. 1. Problem definition.

The continuity equation for incompressible flow is

$$\frac{\partial u}{\partial x}+\frac{\partial w}{\partial z}=0 \tag{3}$$

and the kinematic boundary condition on free surface is

$$\frac{\partial h}{\partial t}+u\frac{\partial h}{\partial x}=w. \tag{4}$$

In the above equations, u and w are, respectively, the fluid velocity components in x- and z-directions, $\ddot{x}_c$ and $\ddot{z}_c$ are the corresponding ground acceleration components, $\dot{\theta}$ and $\ddot{\theta}$ are the pitching angular velocity and angular acceleration, respectively, p is the pressure, h is the free surface height, ρ is the fluid density, g is the gravitational acceleration, and the kinematic viscosity of the fluid is v.

To fulfill the dynamic condition at the free surface, the conservation of linear momentum at the free surface must hold. In brief, the discontinuity in the normal stress are the free surface due to surface tension is proportional to the mean curvature of the free surface, and the continuity of tangential stress condition at the free surface must hold when the fluid is assumed to be viscous. However, the surface tension effect is expected to be small [6] and is neglected in this study. The above conditions can be written as follows [6]:

$$\frac{\partial u}{\partial z}=-\frac{\partial w}{\partial x}+\frac{4\frac{\partial w}{\partial z}\frac{\partial h}{\partial x}}{\left[\left(\frac{\partial h}{\partial x}\right)^2-1\right]}, \tag{5}$$

$$p_0=\rho g(h-d_0)+2\mu\frac{\left[1+\left(\frac{\partial h}{\partial x}\right)^2\right]}{\left[1-\left(\frac{\partial h}{\partial x}\right)^2\right]}\frac{\partial w}{\partial z}, \tag{6}$$

where p_0 is the pressure at free surface and d_0 is the water depth of distill water in tank. Taking partial differentiation of (1) and (2) with respect to x and z, respectively, and summing the results, one can obtain the following pressure wave equation which is used to solve for the pressure:

$$\nabla^2 p=-\rho\frac{\partial}{\partial x}\left(u\frac{\partial u}{\partial x}+w\frac{\partial u}{\partial z}\right)-\rho\frac{\partial}{\partial z}\left(u\frac{\partial w}{\partial x}+w\frac{\partial w}{\partial z}\right)+2\rho\dot{\theta}\left(\frac{\partial w}{\partial x}-w\frac{\partial u}{\partial z}\right)+2\rho\dot{\theta}^2. \tag{7}$$

The no-slip condition is applied at the boundary between fluid and solid, that is $u=0$ and $w=0$ at the tank walls. Consider a contact line being constrained to move across the solid surface with a speed, say U. It is known that the contact angle increases or decreases as the magnitude of U increases according to whether the liquid is advancing or receding [25]. Cox's paper [8] described the manner in which the contact angle varies with the contact line velocity U. This angle is evaluated by calculating the liquid interface shape near the contact line due to the action of the stresses in the liquid produced by the motion. It is also well known that for all contact angles other than 180°, there is a non-integrable singularity in the stress at the contact line that will result in a divergent integral for the drag force on the solid boundary. In order to avoid this problem, slip between the liquid and solid surface has been postulated (see [24,26]) and this assumption removes the non-integrable stress singularity. The treatment of the contact line by Tang et al. [18], which has been successfully applied by both Chen [6] and Huang et al. [12], is adopted here. Tang's assumption states that the no-slip boundary condition is relaxed in the region of the first two nodes on the tank wall beneath the free surface. Since the mesh size near the free surface is stretched, the slip condition is only applied in a very small region, less than 1% of the fluid depth. The results are compared with those based on the assumption invoked by Billinghen [3] in order to verify the size of the stretched region.

3. Coordinate transformation and dimensionless equations

A number of finite difference (FDM) and volume methods have been reported in the literature for solving for the free surface profile of sloshing tanks. The most well-known schemes are SURF, MAC and VOF methods. The SURF scheme assumes a single-valued surface profile and is potentially able to deal with a uniform representation of large free surface waves and even for the inception of overturning. The MAC method is based on Lagrangian concepts and can treat overturning waves and reentry inception with simple logic. In contrast, the VOF method, which is the most popular method used in the literature, tracks the volume occupied by the fluid rather than the free surface. All of the above methods can properly calculate the instantaneous free surface displacement. However, they all require complex computer programming in order to treat the time varying free surface boundary and update the computational mesh. The σ-transformation is also frequently used in treating time varying free surface flows [10,15,17].

In contrast, the present study uses simple mapping functions to remove the time-dependence of the free surface of the fluid domain. The time-varying fluid surface, sloped tank walls and non-horizontal tank bottom can be mapped onto a square by the proper coordinate transformations [22]:

$$x^* = \frac{x - b_1}{b_2 - b_1} \tag{8}$$

and

$$z^* = 1 - \frac{z - d_0}{h(x,t)}, \tag{9}$$

where the instantaneous water surface, $h(x,t)$, is a single-valued function measured from tank bottom, d_0 represents the vertical distance between still water surface and tank bottom, b_1 and b_2 are horizontal distance from the z-axis to the left and right walls, respectively (see Fig. 1). Through Eqs. (8) and (9), one can map the left wall to $x^* = 0$ and right wall to $x^* = 1$, the free surface to $z^* = 0$ and the tank bottom to $z^* = 1$. In this way, the computational domain is transformed to a fixed unit square domain. The main advantage of the transformations is to map a wavy and time-dependent fluid domain onto a time-independent unit square domain. In this model, re-meshing due to the wavy free surface is avoided. Besides, the mapping implicitly deals with the free surface motion, and avoids the need to calculate the free surface velocity components explicitly. Extrapolations are unnecessary and free surface smoothing by means of a spatial filter is not required.

The coordinates (x^*,z^*) can be further transformed such that the layer near the boundary is stretched to capture the sharp local velocity gradients. The following exponential functions provide these stretching transformations:

$$X = \beta_1 + (x^* - \beta_1)e^{k_1 x^*(x^*-1)}, \tag{10}$$

$$Z = \beta_2 + (z^* - \beta_2)e^{k_2 z^*(z^*-1)}. \tag{11}$$

The constants k_2 and β_2 control the mesh size near the free surface and tank bottom. Similarly, the constants k_1 and β_1 map irregular finite difference mesh sizes (Δx^*) near the tank walls to the regular ones (ΔX) in the computational domain (X,Z). Thus, the geometry of the flow field and the meshes in the computational domain (X–Z system) become time-independent throughout the computational analysis. Fig. 2 illustrates the coordinate transformations in the present model.

Finally, the remaining variables can be non-dimensionalized in the following ways. The velocity components are normalized by the long wavelength wave celerity such that $U = u/\sqrt{gd_0}$ and $W = -w/\sqrt{gd_0}$. The pressure, p, is normalized by the hydrostatic pressure $\rho g d_0$ which d_0 is the undisturbed fluid depth, i.e.,

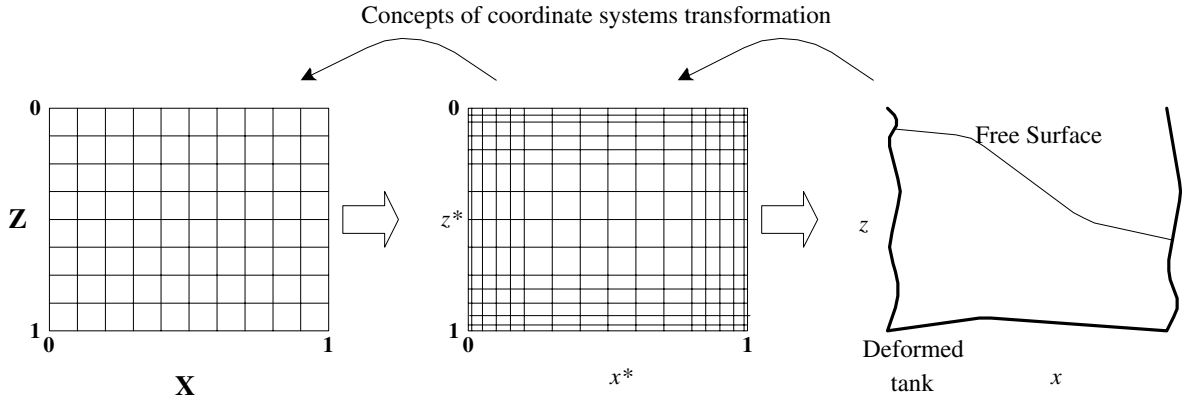

Fig. 2. Concepts of coordinate systems transformation.

$P = p/\rho g d_0$. The dimensionless time is defined to be $T = t\sqrt{g/d_0}$. The fluid depth is normalized by d_0, i.e., $H = h/d_0$, the rotation is normalized as $\Theta = \theta/(2\pi)$, and $X_c = x_c/B$, $Z_c = z_c/B$, where x_c and z_c are the ground displacements in the x and z directions, and B is the tank-width.

With the aforementioned transformations and dimensionless variables, Eqs. (1)–(6) can be written in the following dimensionless forms:

$$\begin{aligned} &U_T + C_5C_7U_X + C_6C_8U_Z + C_1C_7UU_X + C_2C_8UU_Z + C_3C_7WU_X + C_4C_8WU_Z + 4\pi W\Theta_T \\ &\quad = -\sin(2\pi\Theta) - (C_1C_7P_X + C_2C_8P_Z) + C_{10}\Theta_{TT} + C_9\Theta_T^2 - \frac{1}{\lambda}X_{cTT} \\ &\qquad + \frac{1}{Re}\left[\left(C_1C_7\frac{\partial R_1}{\partial X} + C_2C_8\frac{\partial R_1}{\partial Z}\right) + \left(C_3C_7\frac{\partial R_2}{\partial X} + C_4C_8\frac{\partial R_2}{\partial Z}\right)\right], \end{aligned} \tag{12}$$

$$\begin{aligned} &W_T + C_5C_7W_X + C_6C_8W_Z + C_1C_7UW_X + C_2C_8UW_Z + C_3C_7WW_X + C_4C_8WW_Z - 4\pi U\Theta_T \\ &\quad = -\cos(2\pi\Theta) - (C_3C_7P_X + C_4C_8P_Z) + C_9\Theta_{TT} - C_{10}\Theta_T^2 - \frac{1}{\lambda}Z_{cTT} \\ &\qquad + \frac{1}{R_e}\left[\left(C_1C_7\frac{\partial R_3}{\partial X} + C_2C_8\frac{\partial R_3}{\partial Z}\right) + \left(C_3C_7\frac{\partial R_4}{\partial X} + C_4C_8\frac{\partial R_4}{\partial Z}\right)\right], \end{aligned} \tag{13}$$

where

$$\begin{aligned} &R_1 = C_1C_7U_X + C_2C_8U_Z, \quad R_2 = C_3C_7U_X + C_4C_8U_Z, \quad R_3 = C_1C_7W_X + C_2C_8W_Z, \\ &R_4 = C_3C_7W_X + C_4C_8W_Z, \end{aligned}$$

$$(C_1C_7U_X + C_2C_8U_Z) + (C_3C_7W_X + C_4C_8W_Z) = 0, \tag{14}$$

$$H_T + C_5C_7H_X + C_6C_8H_Z + C_1C_7H_XU + C_2C_8H_ZU = -W, \tag{15}$$

$$C_3C_7U_X + C_4C_8U_Z = -(C_1C_7W_X + C_2C_8W_Z) + 4\frac{(C_3C_7W_X + C_4C_8W_Z)(C_1C_7H_X + C_2C_8H_Z)}{\left[(C_1C_7H_X + C_2C_8H_Z)^2 - 1\right]} \tag{16}$$

and

$$p_0 = (H-1) + \frac{2}{R_e}\frac{\left[1+(C_1C_7H_X + C_2C_8H_Z)^2\right]}{\left[1-(C_1C_7H_X + C_2C_8H_Z)^2\right]}(C_3C_7W_X + C_4C_8W_Z). \tag{17}$$

In Eqs. (12), (13) and (17), the Reynolds number R_e is expressed as

$$R_e = \frac{\sqrt{gd_0}d_0}{v}. \tag{18}$$

And the dimensionless pressure wave equation becomes

$$(C_1^2C_7^2 + C_3^2C_7^2)P_{xx} + 2(C_1C_2C_7C_8 + C_3C_4C_7C_8)P_{xz} + (C_2^2C_8^2 + C_4^2C_8^2)P_{zz} = \tilde{\Omega}, \tag{19}$$

where $\tilde{\Omega}$ is

$$\begin{aligned}\tilde{\Omega} = {} & -F^2\{[C_1C_7U_X + C_2C_8U_Z]^2 + [C_3C_7W_X + C_4C_8W_Z]^2 + U[C_1^2C_7^2U_{XX} + 2C_1C_2C_7C_8U_{XZ} \\ & + C_2^2C_8^2U_{ZZ}] + W[C_3^2C_7^2W_{XX} + 2C_3C_4C_7C_8W_{XZ} + C_4^2C_8^2W_{ZZ}] + 2[C_1C_7W_X + C_2C_8W_Z] \\ & \times [C_3C_7U_X + C_4C_8U_Z] + W[C_3C_1C_7^2U_{XX} + C_4C_2C_8^2U_{ZZ} + C_4C_1C_7C_8U_{XZ} + C_3C_2C_7C_8U_{XZ}] \\ & + U[C_3C_1C_7^2W_{XX} + C_4C_2C_8^2W_{ZZ} + C_4C_1C_7C_8W_{XZ} + C_3C_2C_7C_8W_{XZ}] - 4\pi\Theta_T[C_1C_7W_X \\ & + C_2C_8W_Z - C_3C_7U_X - C_4C_8U_Z] - 8\pi^2\Theta_T^2\}.\end{aligned} \tag{20}$$

In the above equations, C_1–C_{10} are the coefficients due to the coordinate transformations and are listed in Appendix I. U_T denotes a partial derivative of U with respect to the dimensionless time; the other terms have similar meanings. For a fully non-linear free-surface condition, the kinematic free surface condition must be applied at the instantaneous free surface location, i.e., at $z = h - d_0$. The coefficients C_1–C_{10} that are related to the free surface position are updated during each iteration of the solution process.

4. Finite-difference method

In this two-dimensional analysis, the fluid flow is solved in a unit square mesh in the transformed flow domain. A staggered grid system is used in the analysis. That is, the pressure P is defined at the center of a cell, whereas the velocity components U and V are calculated $0.5\Delta X$ behind and $0.5\Delta Y$ above the cell center, respectively. The Crank–Nicholson second order finite difference scheme, and the Gauss–Seidel point successive over-relaxation iterative procedure, are used to calculate the velocity and pressure, respectively. A brief description of the numerical procedure is given below. When Eqs. (12), (13) and (15) are considered to be balanced at $T = (n + 1/2)\Delta T$, one can express them in the following finite-difference form:

$$U_{ij}^{n+1} = U_{ij}^{n} - \Delta T[U_{ij}^{c} + U_{ij}^{s} + \wp_{ij}], \tag{21}$$

$$W_{ij}^{n+1} = W_{ij}^{n} - \Delta T[W_{ij}^{c} + W_{ij}^{s} + \overset{5}{\lambda}_{ij}], \tag{22}$$

$$H_{i}^{n+1} = H_{i}^{n} - \Delta T(\Re_{i1} + W_{i1}). \tag{23}$$

In these equations, the superscript n represents the time index (i.e., $T = n\Delta T$). The terms without a superscript are at $T = (n + 1/2)\Delta T$. The velocity components at $T = (n + 1/2)\Delta T$ can be approximated as the mean values between $n\Delta T$ and $(n + 1)\Delta T$. All the terms on the right-hand side of Eqs. (21) and (22) are applied at the same nodes as U_{ij} and W_{ij}. The terms $\wp_{ij}$ and $\overset{5}{\lambda}_{ij}$ are the corresponding pressure gradients in the X and Y directions, respectively. The terms U_{ij}^{s} and W_{ij}^{s} are the corresponding finite-difference expressions for the

viscous terms, the third line of Eqs. (12) and (13). All of the remaining terms in Eqs. (12) and (13) are grouped into U^c_{ij} and W^c_{ij}, which include the finite-difference expressions for the convective acceleration and the terms related to pitch and surge motions. In Eq. (23), $\Re_{ij}$ is the non-linear term of Eq. (15).

The pressure is evaluated by solving the pressure wave equation, Eq. (20). For $T = (n + 1/2)\Delta T$, one can express the finite-difference equation for pressure in the following form:

$$P_{ij} = \frac{\Psi}{a_{ij}}[\Pi_{ij} + \Omega_{ij}] + (1 - \Psi)P^*_{ij}, \tag{24}$$

in which a_{ij} = the sum of coefficients of pressure P_{ij}, Ψ is the relaxation parameter, and P^*_{ij} is the previous iterated pressure. The terms Π_{ij} and Ω_{ij} represent, respectively, the finite-difference expression of the pressure gradient and the non-linear terms. The superscript, $(n + 1/2)$, for P_{ij}, Π_{ij}, and Ω_{ij} are also omitted here. The detailed finite difference expressions for P_{ij} and Π_{ij} are lengthy and are, therefore, omitted from the text. Once the pressure field has been solved by iteration, the velocity components U^{n+1} and W^{n+1} can be calculated from Eqs. (21) and (22), respectively, and the water surface profile H^{n+1} from Eq. (23).

The time step is restricted by the following two conditions:

$$\begin{aligned} &\Delta t < \min\left\{\frac{\Delta x_{\min}}{|u_{i,j}|}, \frac{\Delta z_{\min}}{|w_{i,j}|}\right\}, \\ &v\Delta t < \frac{1}{2}\frac{\Delta x^2_{\min}\Delta z^2_{\min}}{\Delta x^2_{\min} + \Delta z^2_{\min}}. \end{aligned} \tag{25}$$

The first condition states that a fluid particle cannot move more than one cell in a single time step. The second ensures that the diffusion of momentum is not significant over more than one cell in one time step. Besides the constraint on the time-step, another major difficulty faced by the difference scheme is the stretched mesh near the boundary and the accuracy of the second derivative viscous terms. In order to overcome this difficulty, the finite difference approximation of $\partial R_1/\partial X$ requires the evaluation of R_1 at nodes $(i - 1,j)$ and $(i + 1,j)$ and the finite difference expression of $\partial R_1/\partial Z$ requires the evaluation of R_1 at nodes $(i,j - 1)$ and $(i,j + 1)$ to achieve desired accuracy. The detailed finite difference expressions for R_1 in $\partial R_1/\partial X$ and R_1 in $\partial R_1/\partial Z$ are listed in Appendix II. Similar finite difference approximations are made for R_2, R_3 and R_4. The accuracy improvement achieved by the present finite difference approximation is given in Appendix III. The convergence criterion for iteration of U, W and P is 10^{-5}, for H is as small as 10^{-9}.

The detailed implicit iterative solution procedure is given below:

1. Specify the initial conditions.
2. Calculate coefficients C_1–C_{10}.
3. Calculate U^c_{ij}, W^c_{ij}, U^s_{ij} and W^s_{ij}.
4. Substitute the results of step 3 into Eq. (21) in order to calculate Ω_{ij}.
5. Calculate $\wp_{ij}$ and $\lambda^5{}_{ij}$, then substitute the results into left hand side of Eq. (19).
6. Calculate P_{ij} from Eq. (24).
7. Repeat steps 5 and 6 at least 20 times, then check the convergence; that is, check if $|P^{k+20} - P^k| < 10^{-5}$ in which k represents the iteration number.
8. Repeat steps 5–7 until the convergence criterion for P_{ij} is reached.
9. Calculate U_{ij} and W_{ik} from Eqs. (21) and (22), respectively.
10. Check if $|U^{k+1} - U^k| < 10^{-5}$ and $|W^{k+1} - W^k| < 10^{-5}$. If the convergence is not reached, repeat steps 3–10.
11. Calculate H_{ij} by Eq. (23) and check if $|H^{k+1} - H^k| < 10^{-9}$. If the convergence is not reached, go to step 2 and update the coefficients relating to H.
12. If H is converged then begin next time step.

5. Results and discussion

For the purpose of this paper, a fluid system of fixed size (0.9 m tank width and 0.6 m undisturbed fluid depth) is used in most of the simulations. Both surge and pitch excitations are considered in the analysis. The surge motion is given as $\ddot{X}_0 = -X_0\omega_x^2 \sin \omega_x t$ where X_0 = maximum horizontal amplitude and ω_x = surge frequency. The pitch motion is $\ddot{\theta}_0(t) = -\Theta_0\omega_p^2 \cos \omega_p t$ where Θ_0 = maximum angular displacement and ω_p = angular frequency. The stretching factors, $k_1 = k_2 = 5$, are used with a mesh size of 80×80, with the corresponding cell dimensions of $\Delta X = \Delta Y = 0.0125$. A time step of $\Delta T = 0.001$ was determined from the numerical stability requirements, Eq. (25), and a parametric study.

5.1. Viscous effects on sloshing displacement

Fig. 3(a) compares the time-history of the free surface elevation at the right wall of the tank using both a viscous and inviscid analysis, when only surge motions are present. As shown in the figure, the viscous effects significantly reduce the transient amplitude. Fig. 3(b) compares the free surface elevation at the wall when the tank undergoes purely pitch motion, and again significant viscous effects can be seen. Both figures also include the results of an inviscid analysis by Nakayama and Washizu [16]. The agreement between Nakayama's results and those of the present model based on an inviscid assumption is very good.

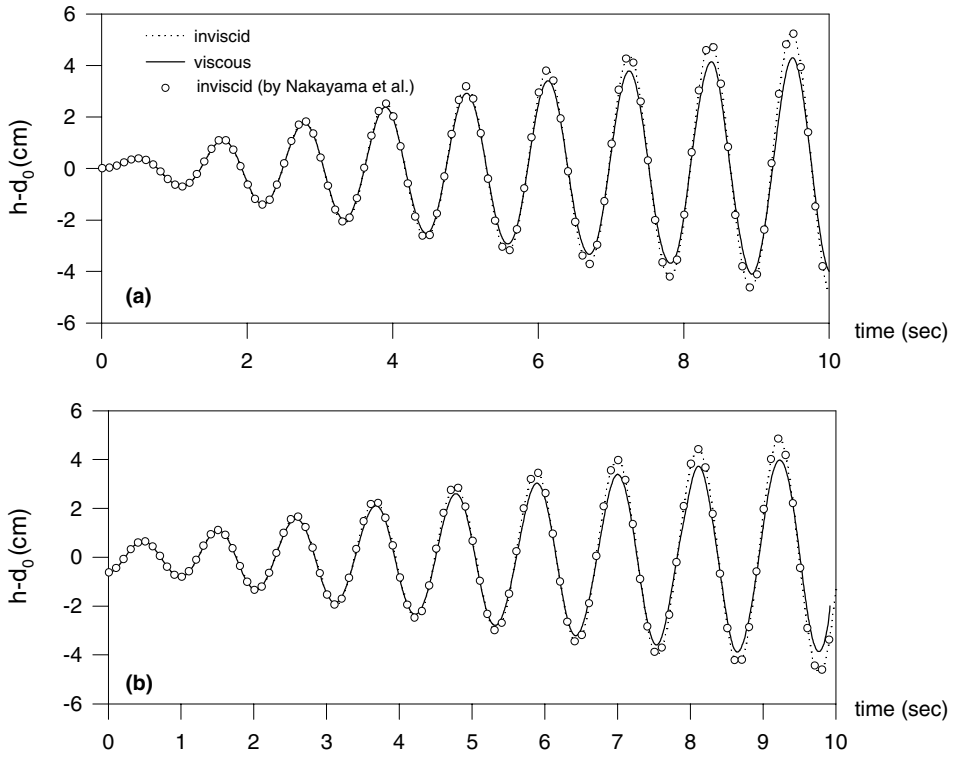

Fig. 3. (a) Under a horizontal ground acceleration, the comparison of the results between viscous and inviscid analyses, $d_0 = 0.6$ m, $B = 0.9$ m. (b) Under a pitch motion, the comparison of the results evaluated by viscous and inviscid analyses, $d_0 = 0.6$ m, $B = 0.9$ m.

Fig. 4 plots the time-history of the free surface elevation at the left wall of the tank under near resonance excitation for $Re = 2000$. The absolute largest sloshing amplitude is observed during the first transient cycle. The maximum amplitude decays during the second and subsequent cycles until finally the system approaches a constant amplitude steady-state. This behavior is known as beating [7]. The maximum transient amplitude is almost twice as large as that of the steady-state response. In a dam-reservoir or tank-storage during an earthquake, this large transient response may cause overtopping or ceiling impact and may constitute a potential hazard. The figure also depicts the sloshing history of a surface wave, obtained from an inviscid analysis. In this case, the largest sloshing amplitude of each wave train is also seen to decline but at a rate much less than that determined by a viscous analysis. Figs. 3 and 4 reveal that the sloshing is significantly affected by viscous effects and clearly viscosity must be included if a realistic simulation of tank sloshing is to be developed.

For the purpose of further validation, the breadth/depth ratio of the tank was chosen to be $L/d_0 = 2.0$. Under harmonic surge motion, the analytical linearized solution of the sloshing displacement η was derived by Faltinsen [9] and Wu et al. [20] as $\eta = \eta_1 + \eta_2$ where:

$$\eta_1 = X_0 \Big/ g\left(x\omega_x^2 + \sum_{n=0}^{\infty} C_n \omega_x \sin k_n x\right) \sin \omega_x t,$$
$$\eta_2 = -X_0 \Big/ g \sum_{n=0}^{\infty} \omega_n (C_n + H_n/\omega_x^2) \sin k_n x \sin \omega_n t \tag{26}$$

and $k_n = (2n + 1)\pi/L$; $\omega_n^2 = g k_n \tanh k_n d_0$; $H_n = \omega_x^3 4/L(-1)^n/k_n^2$, and $C_n = H_n/(\omega_n^2 - \omega_x^2)$. Fig. 5 shows the sloshing displacement at the left wall for various excitation frequencies. The linear analytical solution of Wu et al. [20] and the numerical results of Chen and Chiang [7] (inviscid analysis) are also shown in the figure and the agreement is very good. Under near resonance excitation, Figs. 5(a) and (c) also show beating phenomenon. The frequency of the envelope of the amplitude-modulated wave is $\Delta\omega = |\omega_n - \omega_x|$ and for $\omega_x/\omega_1 = 1.1$ in Fig. 5(a) its period is $2\pi/\Delta\omega$ (=11.82 s), ω_1 the first fundamental frequency. The results for $\omega_x/\omega_1 = 0.999$ yield a very large sloshing amplitude and a very long beat period (=1182 s).

To validate the use of the slip boundary condition for the moving contact line, Fig. 6(a) compares the sloshing displacement predicted using this slip condition to that predicted using Billingham's prescribed

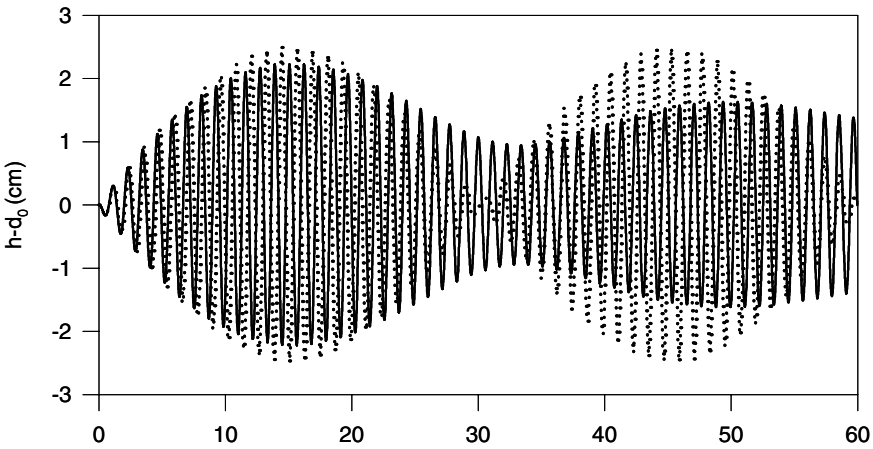

Fig. 4. The comparison of sloshing amplitude with time for constant Reynolds number $Re = 2000$ with surge frequencies $\omega_x = 0.96\omega_1$; solid line: viscous analysis, dotted-line: inviscid analysis.

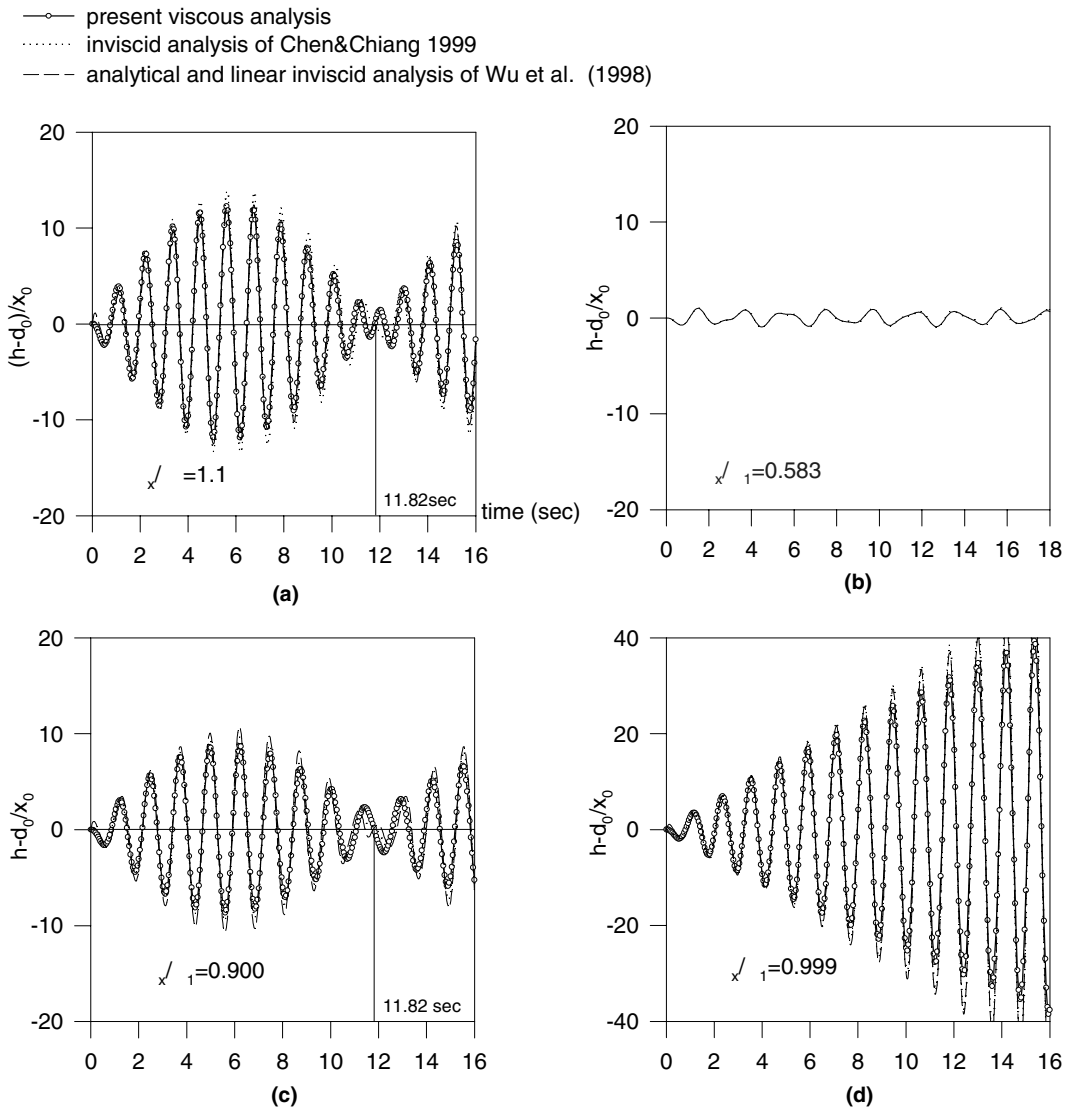

Fig. 5. The comparison of sloshing free surface at left wall for different surge frequencies, $X_0(t) = -X_0\omega_x \cos\omega_x t$, $X_0/d_0 = 0.00186$; ω_x/ω_1 = (a) 1.1, (b) 0.583, (c) 0.9 and (d) = 0.999.

function, i.e., $\partial h/\partial t = \lambda \partial h/\partial x$. Three different values were chosen for the parameter λ in Billingham's function, namely $\lambda = 0.1$, 1, and 4. As shown in the figure, the results of the present study agree well with those using Billingham's assumption when $\lambda = 1$ and 4. However, when a value of $\lambda = 10$ was selected, the simulation was divergent. The reason for this behavior may be due to the velocity at the contact line being too much larger than that of the water at the ambient free surface.

The effect of the mesh stretching factor, k_1, is illustrated in Fig. 6(b) where the sloshing displacement at the left wall is shown for $k_1 = 5$ and $k_1 = 10$. The difference between the predictions of the two simulations is negligible.

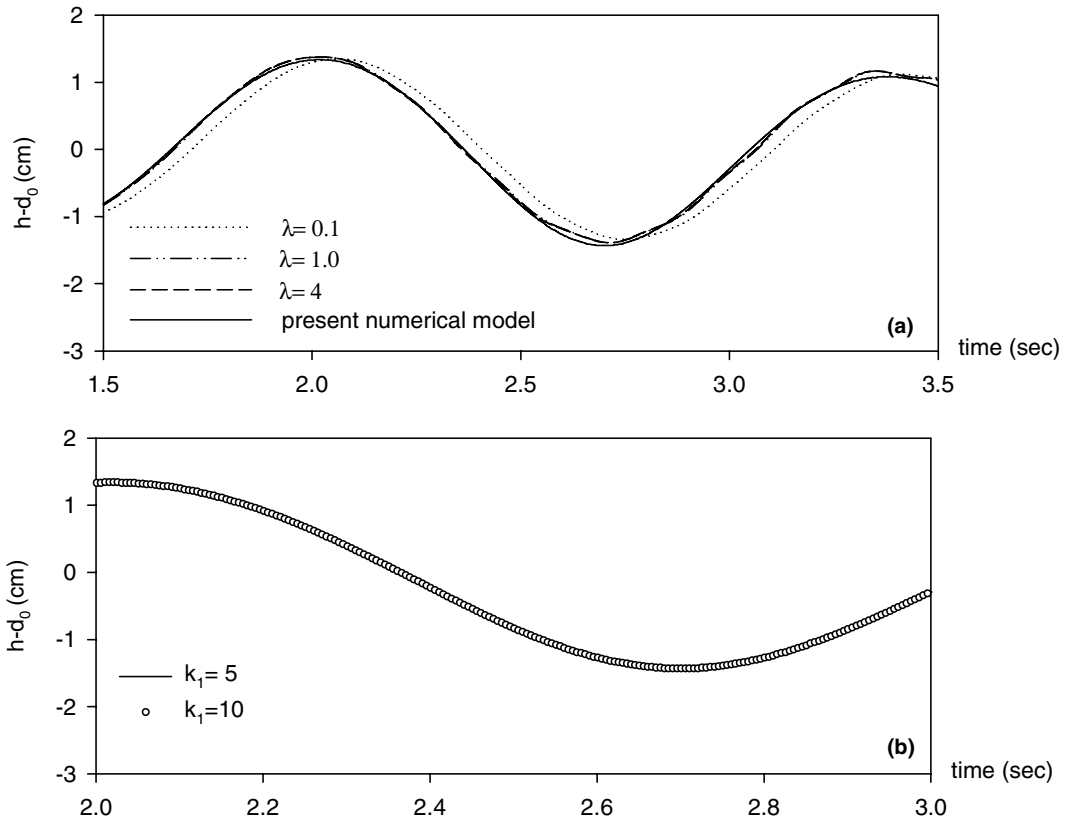

Fig. 6. (a) The comparison of the sloshing displacement at left wall due to different moving contact line. (b) The comparison of the sloshing displacement at left wall due to various stretch parameters.

5.2. Frequency dependence and Reynolds numbers effects on sloshing amplitude

The free surface elevation at the right wall under only surge conditions is plotted in Fig. 7 for a range of excitation frequencies, ω_x. The surface elevation on the left wall is almost negligible when the excitation frequency is below $0.69\omega_1$. Fig. 8 shows the maximum end wall free surface displacement as a function of the relative forcing frequency and clearly demonstrates the occurrence of resonance for sloshing fluid in tank under a surge motion. The first resonant peak is shifted to the left of the first fundamental mode (assuming an ideal fluid) due to the non-linearity of the fluid sloshing and also the effect of the viscosity of the fluid. A more detailed discussion of this phenomenon can be found in Hill [11].

Fig. 9 plots the absolute transient surface displacement at the left wall as a function of Reynolds number for various surge frequencies. Here the Reynolds number is defined to be $Re = u_0 d_0/\upsilon$ where the maximum surge velocity is $u_0 = x_0\omega_x$. The figure shows that the peak surface elevation increases almost linearly with Reynolds number for a given frequency of excitation. For a fixed frequency, ω_x, the Reynolds number is proportional to the surge amplitude. The peak surface elevation is, therefore, proportional to the amplitude of the surge motion. However, for a constant Reynolds number, the peak surface elevation varies with frequency.

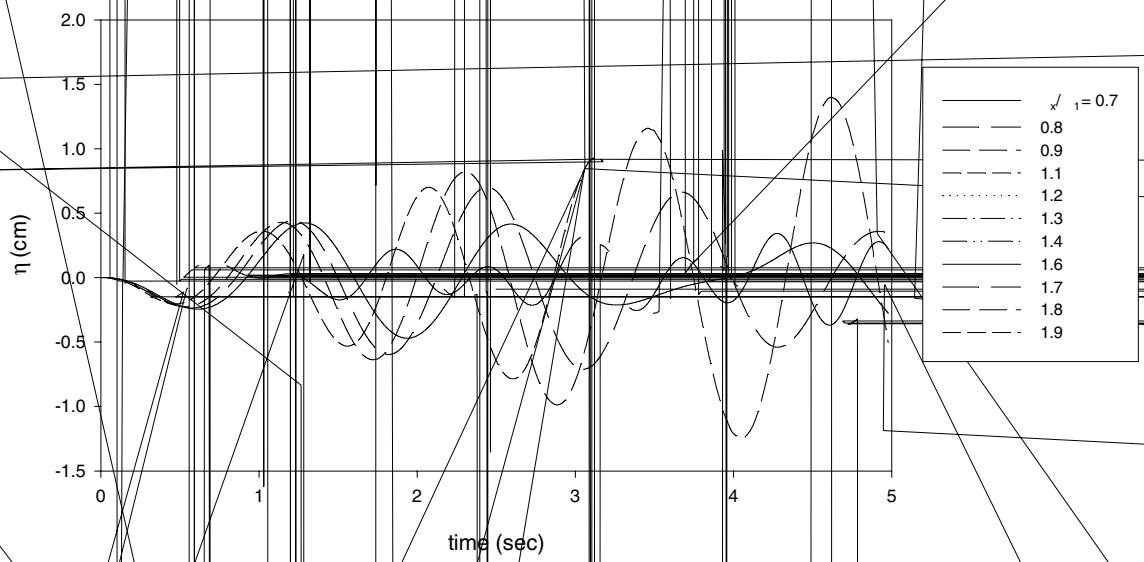

Fig. 7. Free surface elevation at left wall under surge motion with various exciting frequencies.

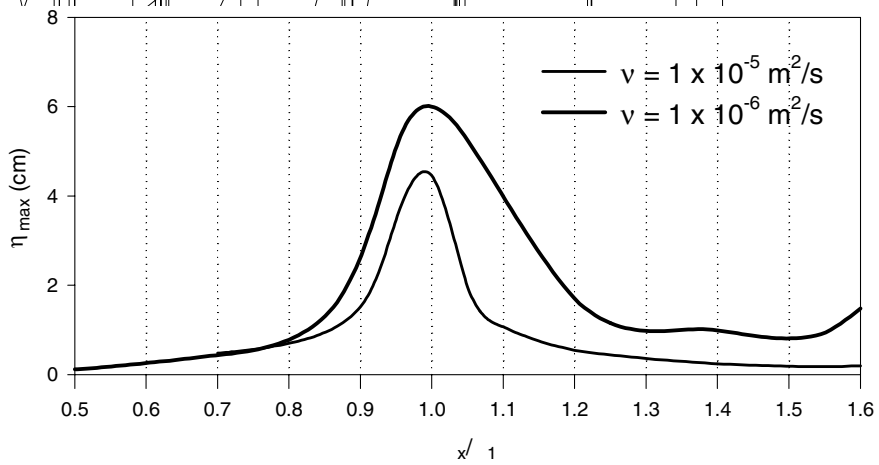

Fig. 8. The maximum transient end wall displacement with various exciting frequencies and different fluid viscosity.

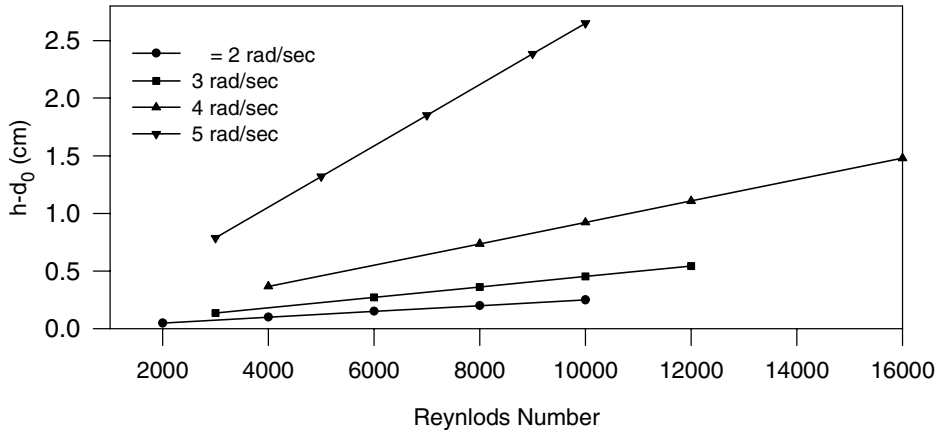

Fig. 9. The peak surface elevation at left wall versus Reynolds numbers for various exciting frequencies.

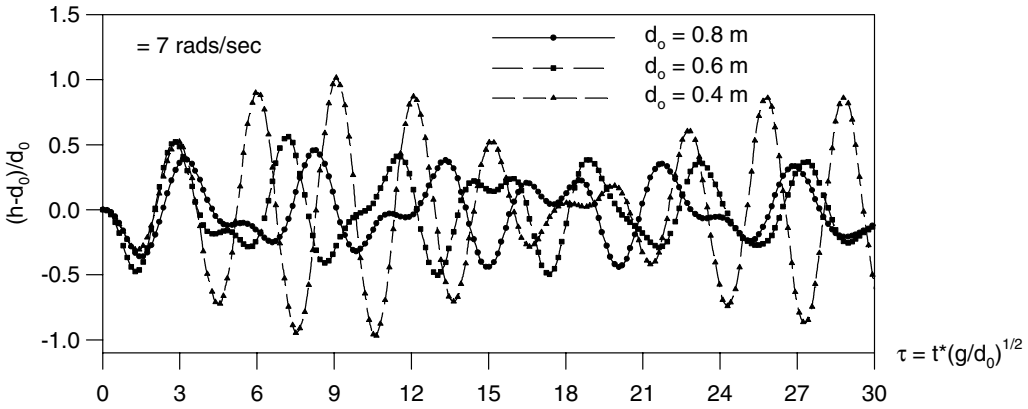

Fig. 10. Free surface elevation at left wall under surge motion, for constant exciting frequencies with various water depth.

elevation during tank motion. In this section, several simulations are carried out to study the coupling effects, vertical excitation effects and the effects of initial surface conditions on the sloshing displacements. The surge motion is given as $\omega_x/\omega_1 = 0.7$, and $a_x(t) = -0.0036g\cos(\omega_x t)$, the heave motion is given as $\omega_1/\omega_h = 1.253$, $\eta(x,t=0) = a\cos(k_n x)$, $k_n = \pi/B$, $a_z(t) = -0.5g\cos(\omega_h t)$ and $a\omega_1^2/g = 0.0014$; and the pitch motion is given as $\omega_p/\omega_1 = 0.8$, $a_p(t) = -0.005g\cos(\omega_h t)$. Fig. 11 compares the free surface variations at the left wall under different combinations of ground excitation. Figs. 11(a)–(c) are, respectively, the surface elevations at the left wall of the tank under solely surge, heave and pitch motion, respectively. Fig. 11(d) shows the surface elevation due to coupled surge and heave motion, together with a linear superposition of the results evaluated from independent surge and heave motion. The initial free surface is a cosine shape. Significant differences between the coupled and superimposed motions are evident, providing strong evidence for the importance of the non-linear flow characteristics [7]. Fig. 11(e) depicts the corresponding results for surge and pitch motions. Differences between the two motions are insignificant indicating that the coupling, in this case, is insignificant. The case of the complete 2D excitation due to coupled surge, heave and pitch motions, is plotted in Fig. 11(f), and significant coupling effects are again noted.

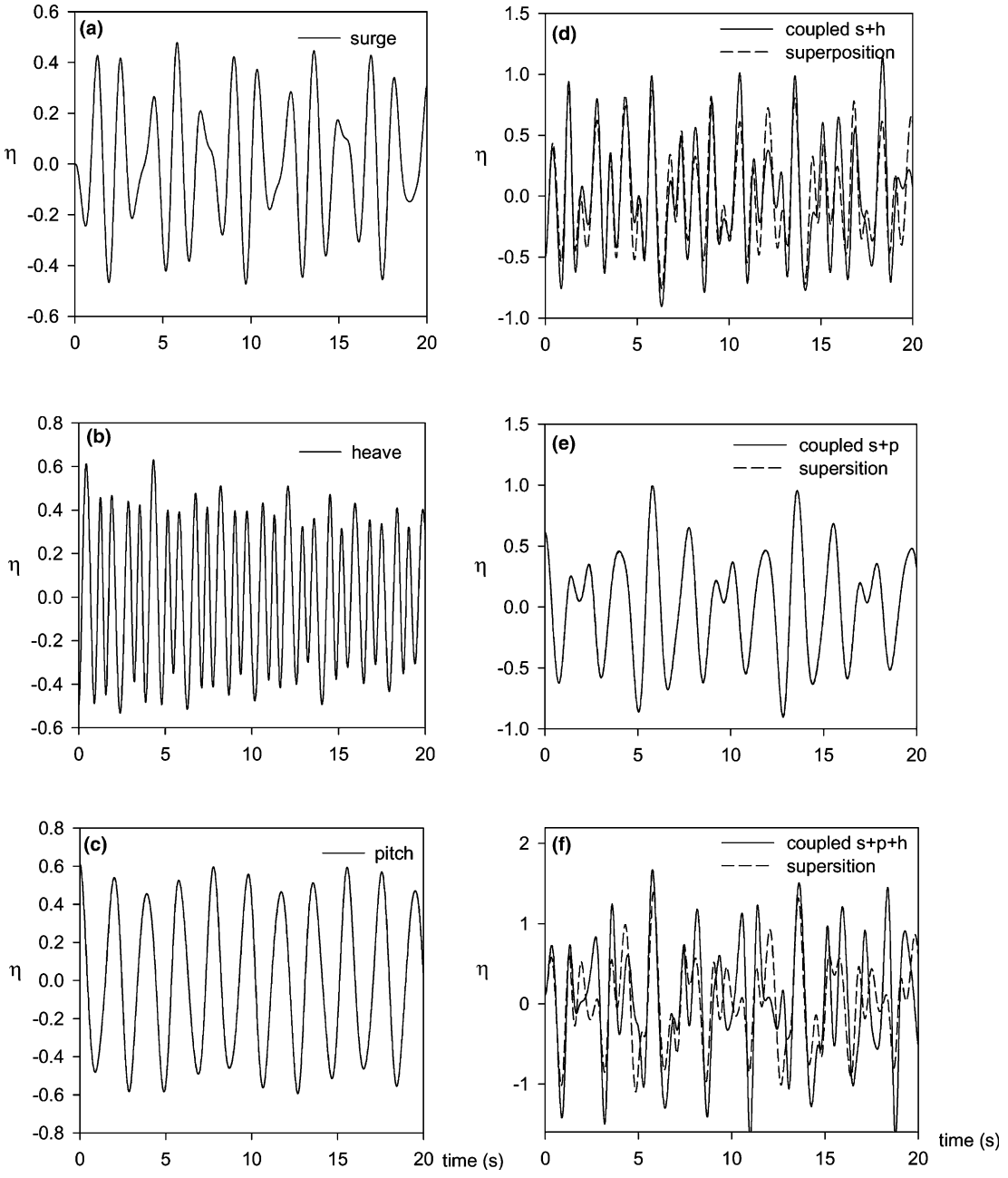

Fig. 11. The coupling effects of simultaneous action of surge, heave and pitch motions.

The effect of the initial free surface condition is illustrated in Fig. 12. Fig. 12(a) compares the surface elevation due to coupled surge and heave motions with different initial surface conditions. The sloshing displacement of a surface with an initial cosine shape is much larger than that with an initially plane surface. Assuming an initial plane surface, Fig. 12(b) plots the surface elevation at the left wall due to surge motion

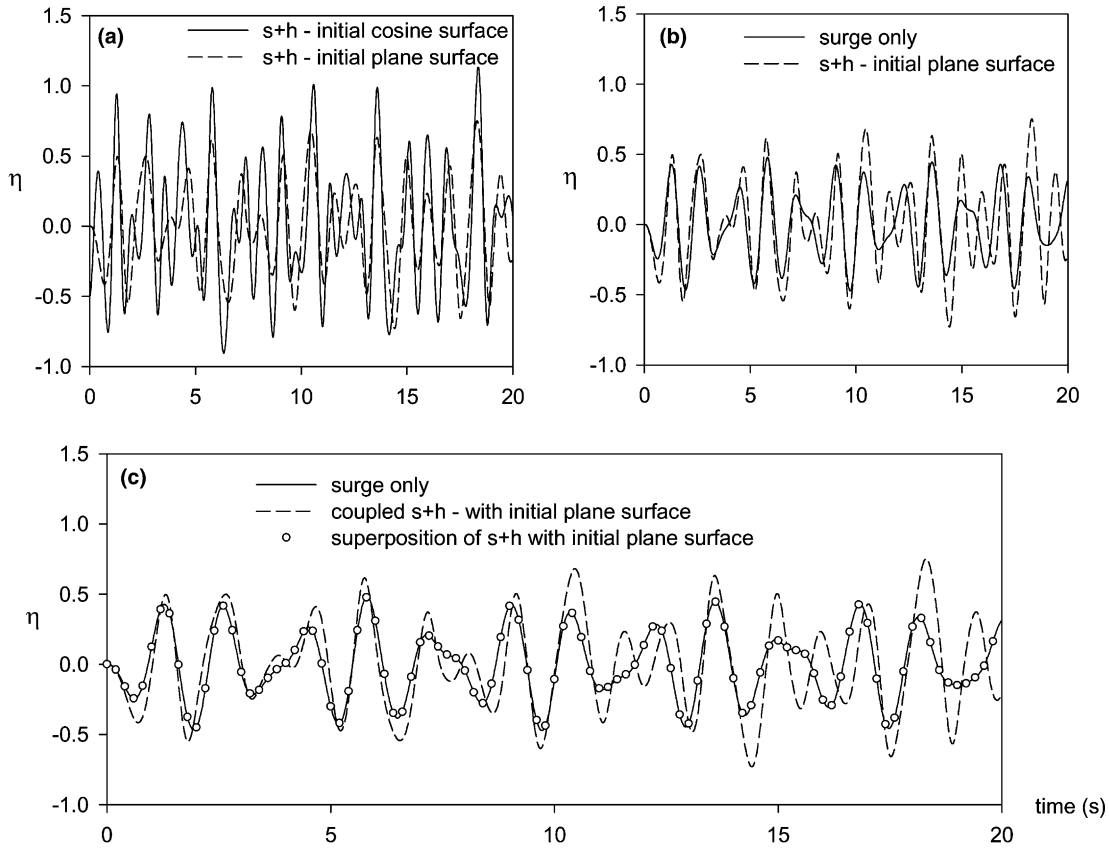

Fig. 12. The effects of initial free surface; (a) the comparison of surface elevation at left wall by coupled surge and heave motions with different initial free surface; (b) surface elevation at left wall by surge motion only and by coupled surge and heave motions with initial plane surface; (c) the comparison of surface elevation by coupled surge and heave motions and by superposition of separate motion with initial plane surface.

alone and also the elevation due to coupled surge and heave motions. No significant variation is observed before $t = 5$ s but pronounced differences occur once a large surface disturbance has been generated and the vertical excitation enhances the disturbance initially generated by the surge motion. The vertical excitation changes the acceleration of gravity and also varies the Froude number which is closely related to the variation of the surface elevation. The significance of vertical excitation on tank sloshing was also reported in Frandsen [10]. For an initially plane surface, vertical excitation alone does not generate any surface disturbance. Fig. 12(c) shows no difference between the superposition of surface sloshing of independent surge and heave motion and the surface elevation generated by single surge motion.

5.4. Evolution of velocity vectors

Fig. 13 shows the evolution of fluid velocity in the tank for two times, $t = 3.85$ and 4.1 s, under a horizontal excitation. At $t = 3.85$ s, the free surface profile has a positive gradient and the free surface elevation at the right wall reaches its peak, with the fluid velocity almost zero. After $t = 3.85$ s, the direction of the fluid velocity switches from rightward to leftward and the magnitudes of the velocities continue to increase until they reach their maximum values at $t = 4.1$ s and the fluid surface is a horizontal plane. Thereafter, the

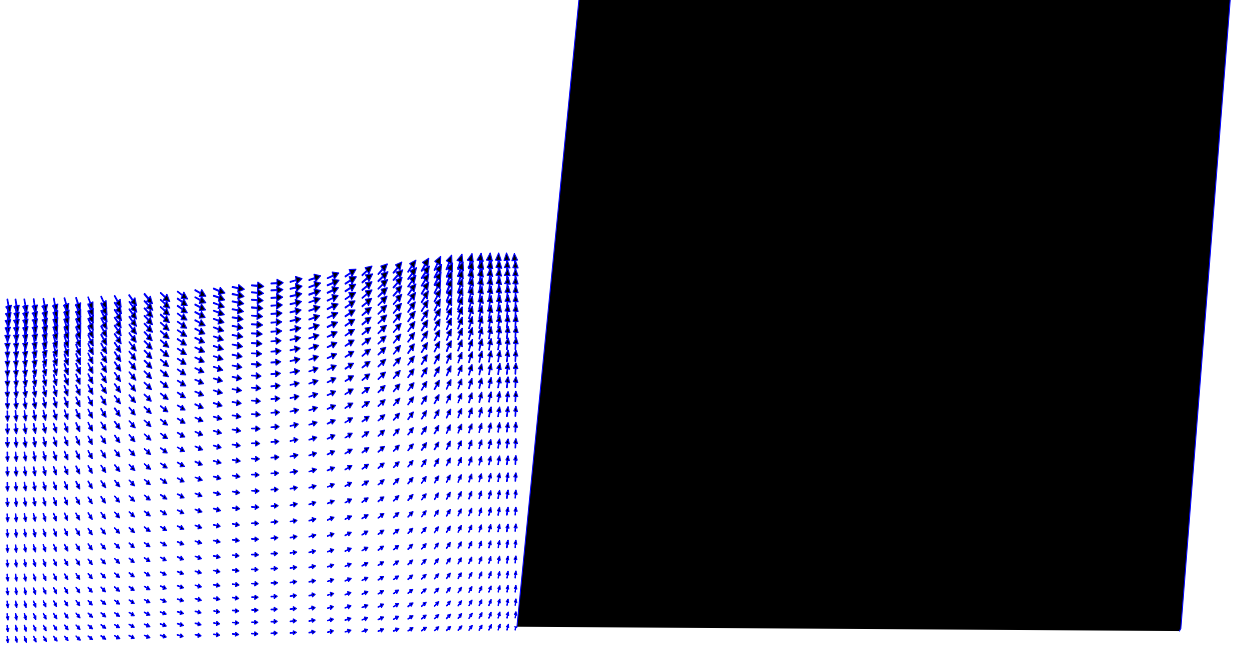

fluid surface has a negative gradient. There are no obvious eddies shown in the tank during this surge excitation.

The evolution of the velocity in the tank under simple pitch motion is plotted in Fig. 14. Under surge motion, the fluid velocity at the tank walls becomes zero when the surface profile at the left or right wall is a peak. When the tank is excited by a pitch motion, the velocities at the tank walls do not vanish but constantly rotate when the surface elevations at both walls are a peak or trough. At $t = 4.75$ s, the clockwise rotating momentum creates a clear clockwise circular eddy in the upper part of the tank. As shown in the figure, fluid in the upper part of the tank moves to the right and parallel to the free surface, except for the fluid in the upper right corner. The surface elevations at both walls stop increasing and decreasing. Just 0.05 s later, at $t = 4.8$ s, the eddy is compressed by the rotating free surface and its shape becomes elliptical. In a very short time, the eddy keeps sinking as the velocity of the right moving fluid in the upper part of the tank significantly increases, and the velocity vectors at the left wall switch direction from upward to downward. However, the velocities in the right upper corner do not change direction, and continue to point downward. At $t = 4.85$ s, the elliptical eddy is further stretched and split into two eddies, where the counterclockwise rotating fluid occupies most of the fluid field. The surface becomes a horizontal plane again at $t = 5.045$ s and the separated eddies vanish. Part of the fluid is confined to the lower part of the tank due to the sinking eddies and thus the eddy effectively reduces the surface elevation in the tank.

More detailed information about the fluid motion due to pure pitching motion can be garnered from the plots of flow streamlines depicted in Fig. 15. The table listed in the figure indicates the time of each streamline pattern. Also shown in the figure is the time series of the free surface displacement at the left wall from $t = 4$–5.5 s. At $t = 4.2$ s, the surface elevation at the left wall is a trough and the surface displacement on both walls will cease rising or falling, and will start to change direction. The clockwise rotating surface profile is associated with the pitch forcing and creates a clear clockwise eddy at the upper part of the tank. This eddy sinks very quickly and is depressed by the rocking free surface. The surface gradient decreases from maximum positive to zero and then to maximum negative. The eddy sinks further, splits into two parts, and vanishes when the free surface becomes a horizontal plane. No eddy reappears until the free surface elevation at the left wall increases to a peak value and starts changing direction. At this point, a clear

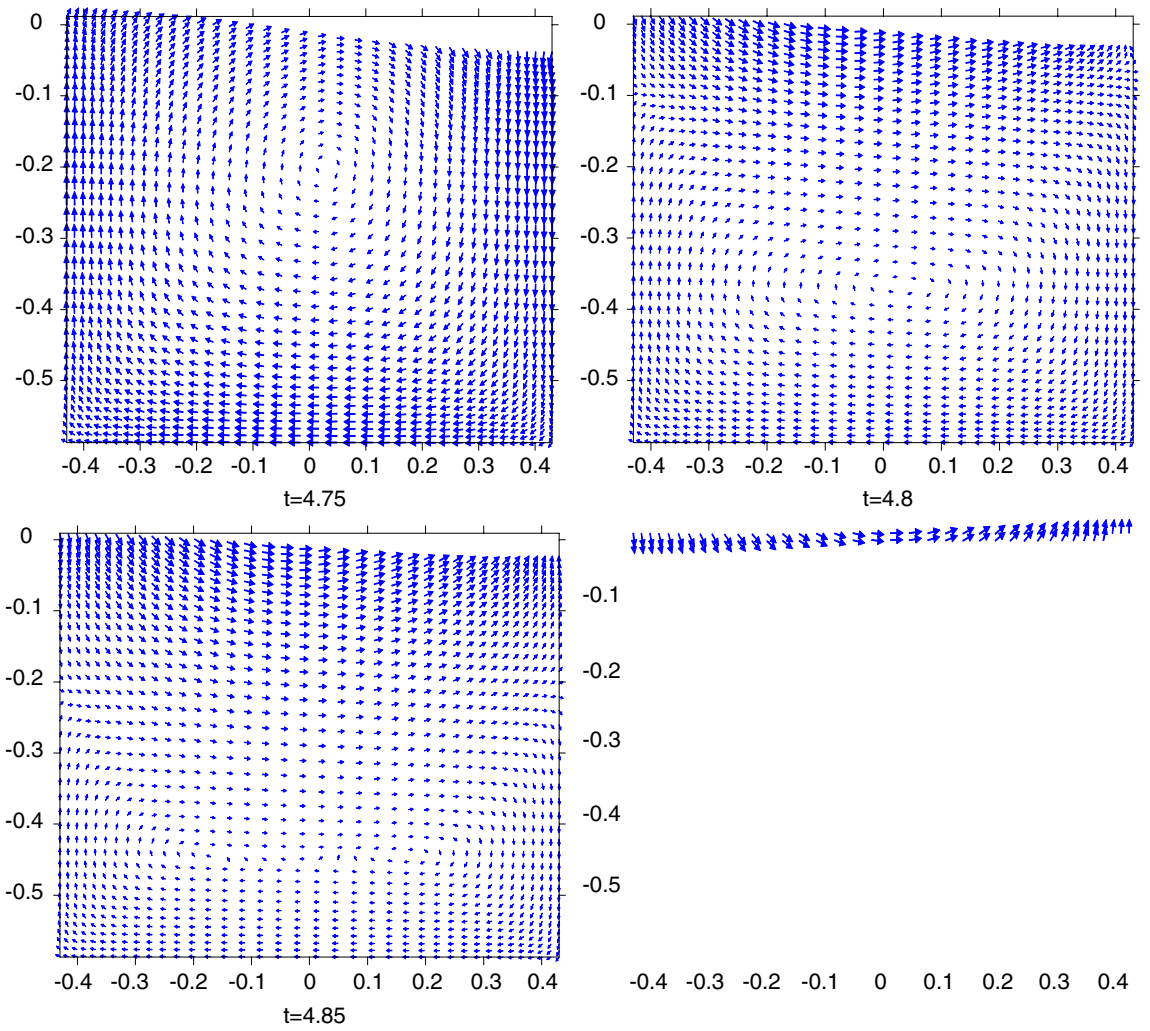

counterclockwise eddy appears in the upper part of the flow. This eddy will also sink, split and disappear when the free surface returns to a horizontal plane.

The streamline patterns generated by coupled surge and pitch motions are now considered. Two cases are studied in this section. The first case assumes the acceleration of the surge motion is $a_x(t) = -a\sin(\omega_x t)$, and that of pitch motion is $a_p(t) = -a\cos(\omega_p t)$, $\omega_x = \omega_p$. And the second case assumes $a_x(t) = +a\sin(\omega_x t)$, and that of pitch motion is $a_p(t) = -a\cos(\omega_p t)$, $\omega_x = \omega_p$. The streamline patterns for both cases are shown in Fig. 16. A very interesting phenomenon is found in the first case. At $t = 3.74$ s, the free surface elevation at the left wall is a peak, and the free surface profile has a maximum negative gradient. The eddy in the upper portion of the tank sinks, but it does not disappear as the free surface becomes a horizontal plane. Instead the split eddies start to merge and rise when the gradient of the surface profile becomes positive. The eddy keeps rising and finally vanishes at the tank surface when the surface elevation at the left wall becomes a trough, and the eddy does not reappear until the surface elevation at the left wall of the tank becomes a peak again.

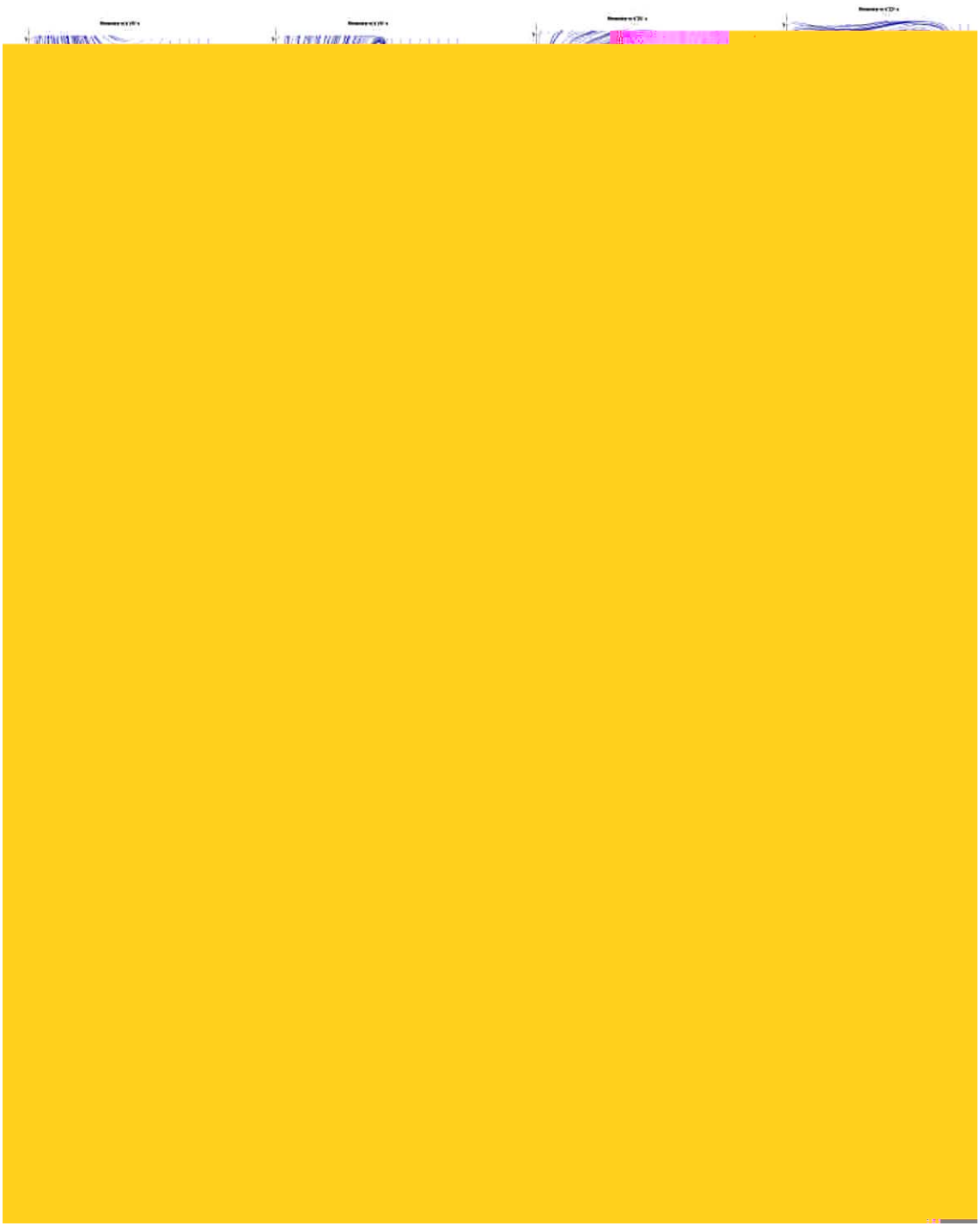

Fig. 15. The streamline patterns of the sloshing fluid in a tank under pitch motion.

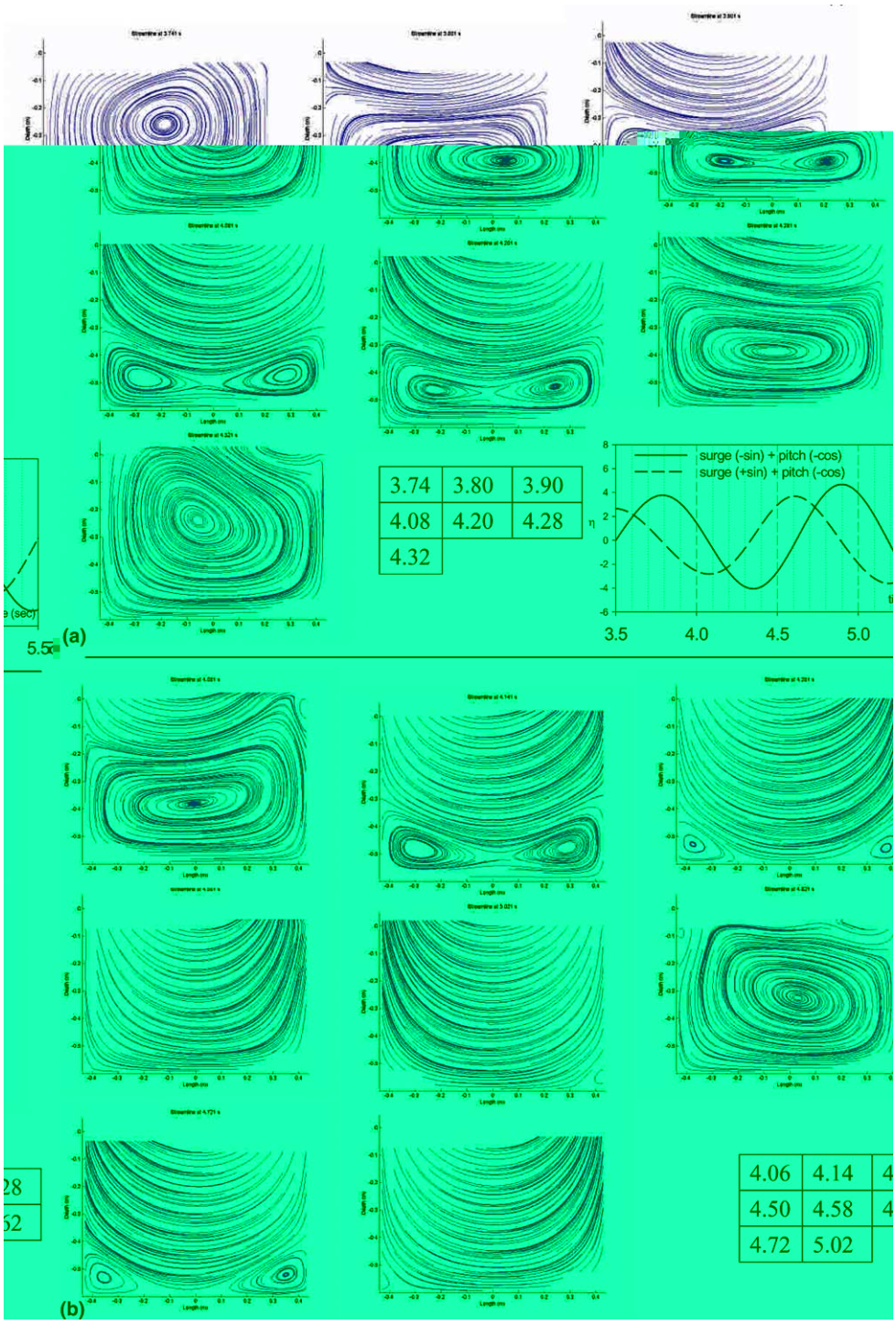

Fig. 16. The streamline patterns of coupled surge and pitch case (a) the upper parts: surge (−sin) + pitch (−cos); (b) the lower parts: surge (+sin) + pitch (−cos).

In the second case, the streamline pattern development is similar to that of the tank excited solely by pitch motion. In the first case, the eddies exist for approximately three quarters of one sloshing cycle, while in the second case it is only present over half a cycle. The eddy could enhance the fluid mixing in the tank. Thus, the tank sloshing due to coupled surge and pitch motion in the first case may cause better fluid mixing than when the tank is excited by pitch motion alone or by the second combination of coupled pitch and surge motion.

The streamline patterns for a tank excited by coupled surge, pitch and heave motions are illustrated in Fig. 17. The forcing accelerations of the pitch and surge motions are the same as the second combination of the previous investigation. Similar phenomenon to those due to pitch motion alone can be seen and the inclusion of heave motion does not significantly increase the fluid mixing during tank sloshing.

5.5. Hydrodynamic force coefficients

The forces acting on the tank are attributed to pressure and viscous stresses. The viscous stresses are parallel to the wall and the normal force on the wall is, therefore, primarily attributed to the hydrodynamic pressure. In the moving coordinate system, the normal velocity of water at the tank wall is zero, and the pressure gradient normal to the tank wall during surge motion can be written as

$$\frac{1}{\rho}\frac{\partial p}{\partial x} = -\ddot{x}_c.$$

According to the added mass concept, [30], the pressure along the tank wall under surge acceleration can be assumed to be

$$p(z) = -\rho \ddot{x}_c x_e(z) + C, \tag{27}$$

where $x_e(z)$ is the effective length of water accelerated during tank motion and C is an integration constant to be determined. The dynamic free surface boundary condition indicates

$$p(z = h - d_0) = \rho g(h - d_0) + 2\mu \frac{\left[1 + \left(\frac{\partial h}{\partial x}\right)^2\right]}{\left[1 - \left(\frac{\partial h}{\partial x}\right)^2\right]} \frac{\partial w}{\partial z}. \tag{28}$$

For simplicity, we may assume $\partial h/\partial x < 1$ and $x_e(z = h - d_0) = 0$, thus, $C = \rho g(h - d_0) + 2\mu \frac{\partial w}{\partial z}$, and we have

$$p(z) = -\rho \ddot{x}_c x_e(z) + \rho g(h - d_0) + 2\mu \frac{\partial w}{\partial z}. \tag{29}$$

If the hydrodynamic force coefficient is defined to be $C_F = \int p \, dz/\rho g d_0^2$, then

$$C_F = \rho x_0 \omega_x^2 \sin \omega_x t \int_0^h x_e(z) \, dz/\rho g d_0^2 + (h - d_0)h/d_0^2 + 2\mu \frac{\partial w}{\partial z}_{(z=h-d_0)} h/\rho g d_0^2. \tag{30}$$

The first term is attributed to the added mass effect; the second term to the kinematic free surface displacement, and the last term to the effects of viscosity on the free surface wave. This final term is expected to be small as $\partial w/\partial z \sim 0$ due to the non-slip boundary condition at the tank wall. We can see from Eq. (30) that the hydrodynamic force coefficients are dominated by the free surface displacement when the excitation surge frequency is small, and are dominated by the added mass effect when the surge frequency is large. These effects on C_F are combined at a medium excitation frequency.

Fig. 18 plots the time histories of surface displacement at the left wall of the tank under surge motion for various excitation frequencies. Fig. 19 shows the corresponding histories of hydrodynamic force coefficients. Comparing these two figures, it can be observed that the hydrodynamic force coefficients are linearly related to the sloshing surface displacement when the surge frequency, ω_x, is less than ω_1. In

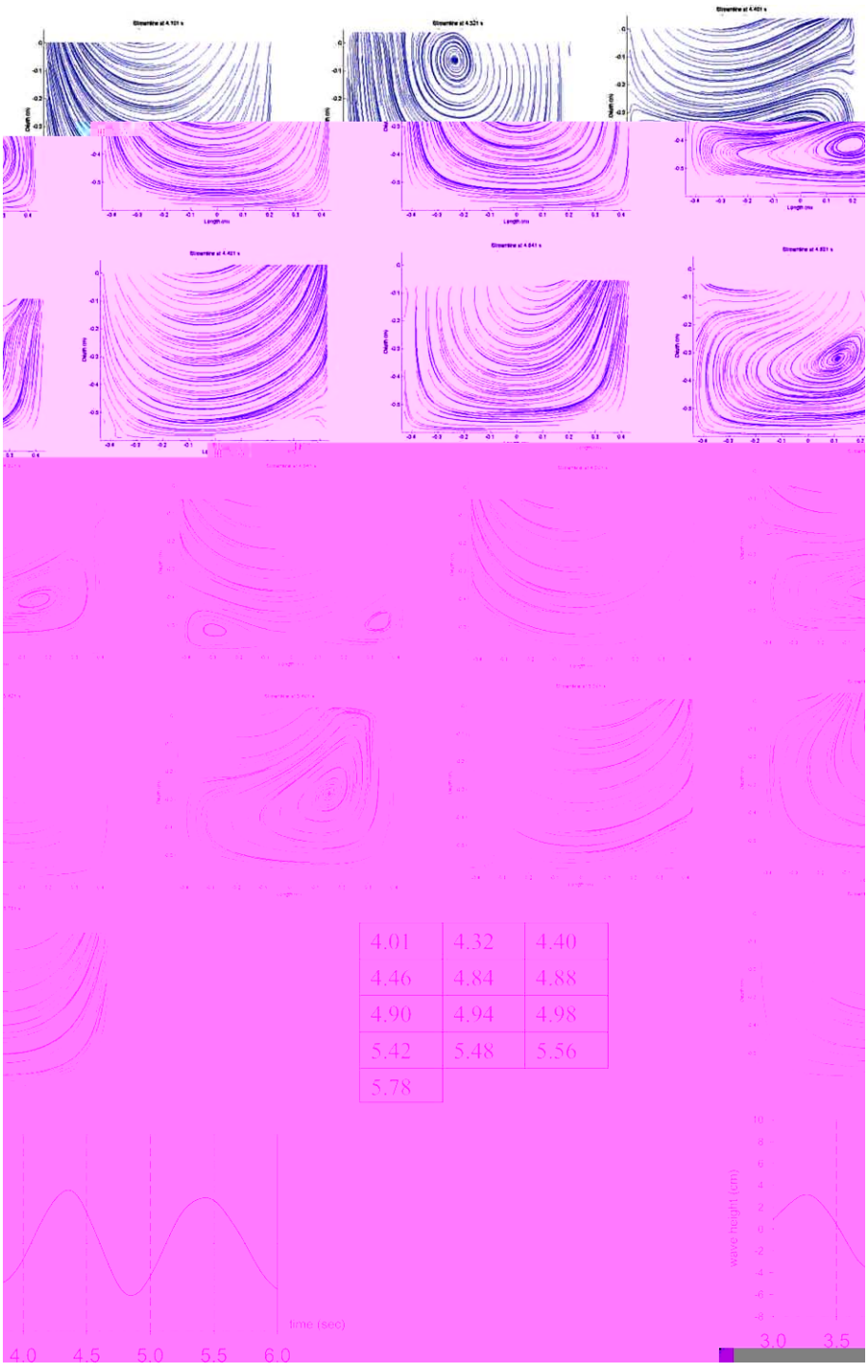

Fig. 17. The streamline patterns of the sloshing fluid in a tank under coupled surge, pitch and heave motions.

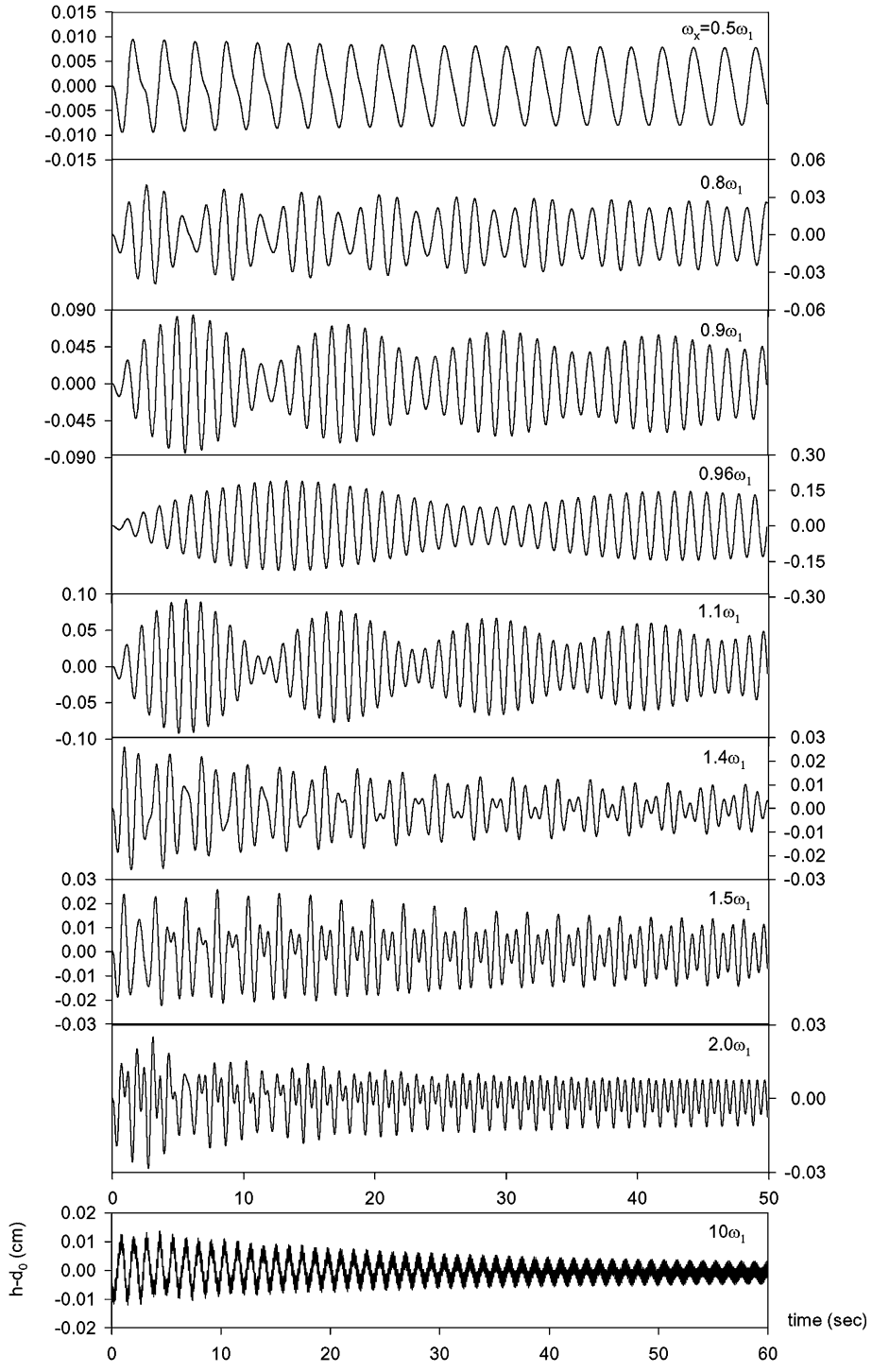

Fig. 18. Under surge motion, the time-history of surface displacement at left tank wall with various exciting frequencies.

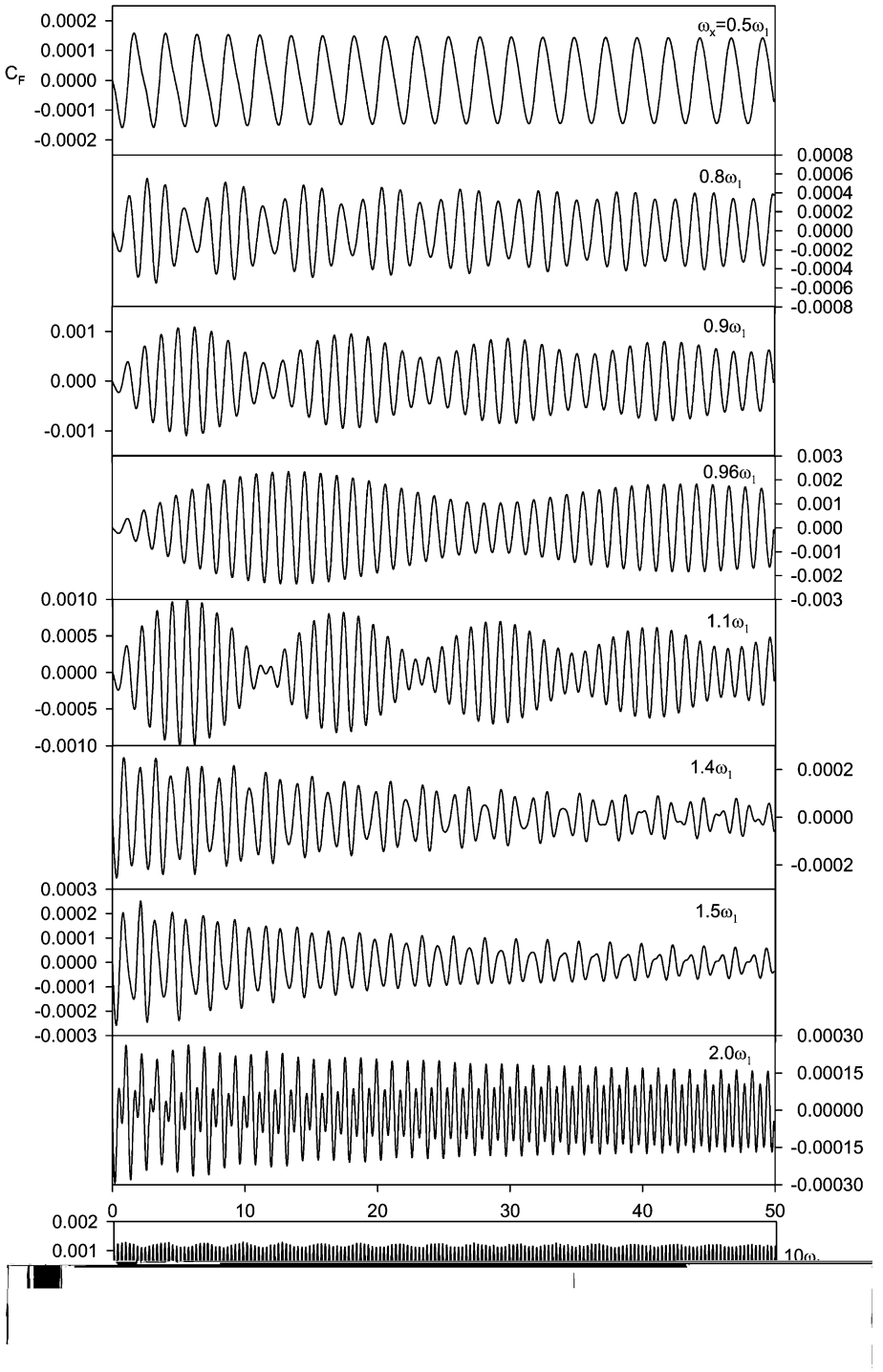

Fig. 19. Under surge motion, the time-history of hydrodynamic force coefficient acting on left tank wall, with various exciting frequencies.

dam hydrodynamics, the free surface wave effects are negligible and the ratio of the hydrodynamic force coefficients to the acceleration due to excitation is a constant (=0.525, [7,23]). Fig. 20 further compares the numerically calculated hydrodynamic force coefficients with those evaluated by Eq. (30). For the

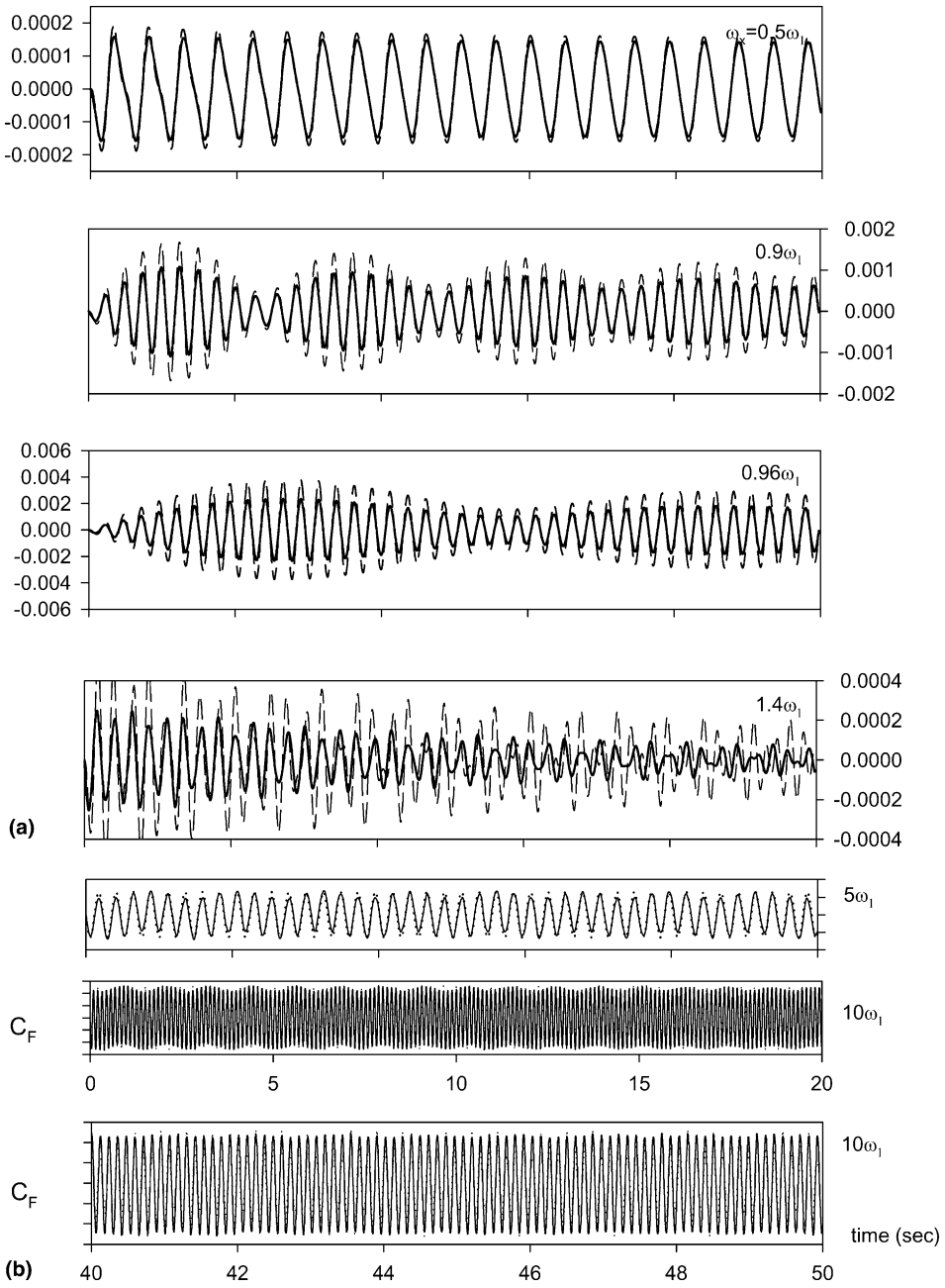

Fig. 20. (a) Under surge motion, the time-history of hydrodynamic force coefficient acting on left tank wall, $Re = 200$. Solid line: calculated C_F, dashed line: $\eta h/d_0^2$. (b) Under surge motion, the time-history of hydrodynamic force coefficient acting on left tank wall, $Re = 200$. Solid line: calculated C_F, dotted-line: $0.525a_x(t)/g$; $a_x(t)$: surge-acceleration.

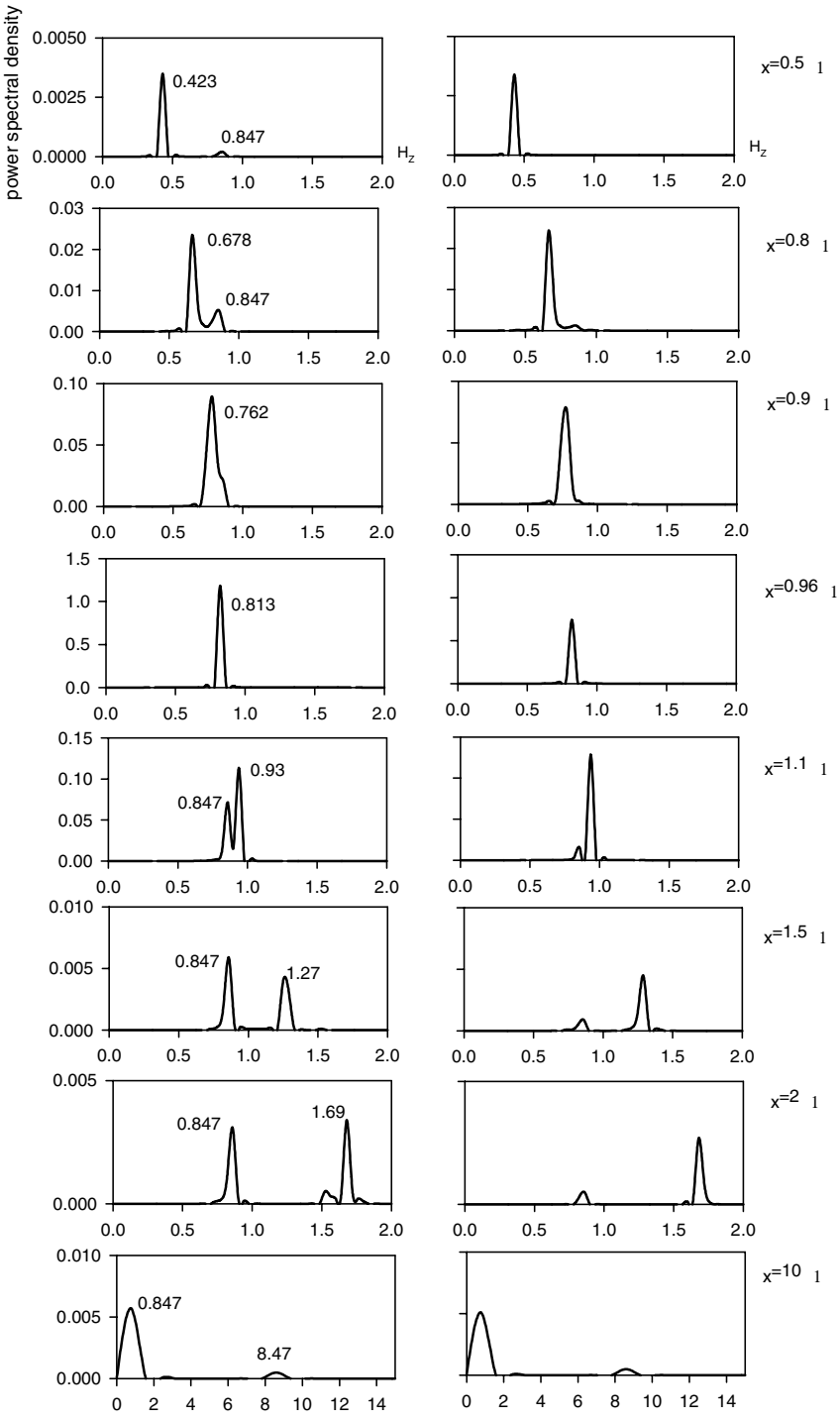

Fig. 21. Under surge motion, the power spectral density versus frequency of the time-history of sloshing displacement, with various exciting frequencies ω_x.

third plot of Fig. 20(b), the frequency of excitation ω_x is as large as $10\omega_1$ and the ratio of C_F to $a_x(t)$ is ≈ 0.525.

5.6. FFT analysis of sloshing displacement

A fast Fourier transform (FFT) provides a spectral analysis of the sloshing motion in the tank and enables the dominant response frequencies of the system to be identified. Fig. 21 illustrates the power spectral density as a function of frequency for the sloshing displacements under various excitation frequencies. The left and right columns of figures are the power spectral density for two sloshing periods ($t = 0$–10 s) and ($t = 40$–50 s), respectively. As can be seen in the top two graphs in Fig. 21, the dominant frequencies of the sloshing displacement are, respectively, 0.423 and 0.678 Hz. These are exactly equal to the frequencies of excitation, $0.5\omega_1$ and $0.8\omega_1$. However, the first fundamental frequency of the water in the tank, which is equal to 0.847 Hz, plays a less important role in the system. When the frequency of excitation is less than the first fundamental frequency of the system, the water in the tank has enough time to pick up the external excitation and the frequency of the sloshing surface displacement is, therefore, controlled by the frequency of the external excitation.

As the frequency of excitation nears, but is still less than the fundamental frequency ω_1, no second peak appears. When ω_x is equal to $1.1\omega_1$, the external excitation frequency still dominates the frequency of the sloshing displacement throughout the time history. As ω_x increases to $1.5\omega_1$ and $2\omega_1$, the fundamental

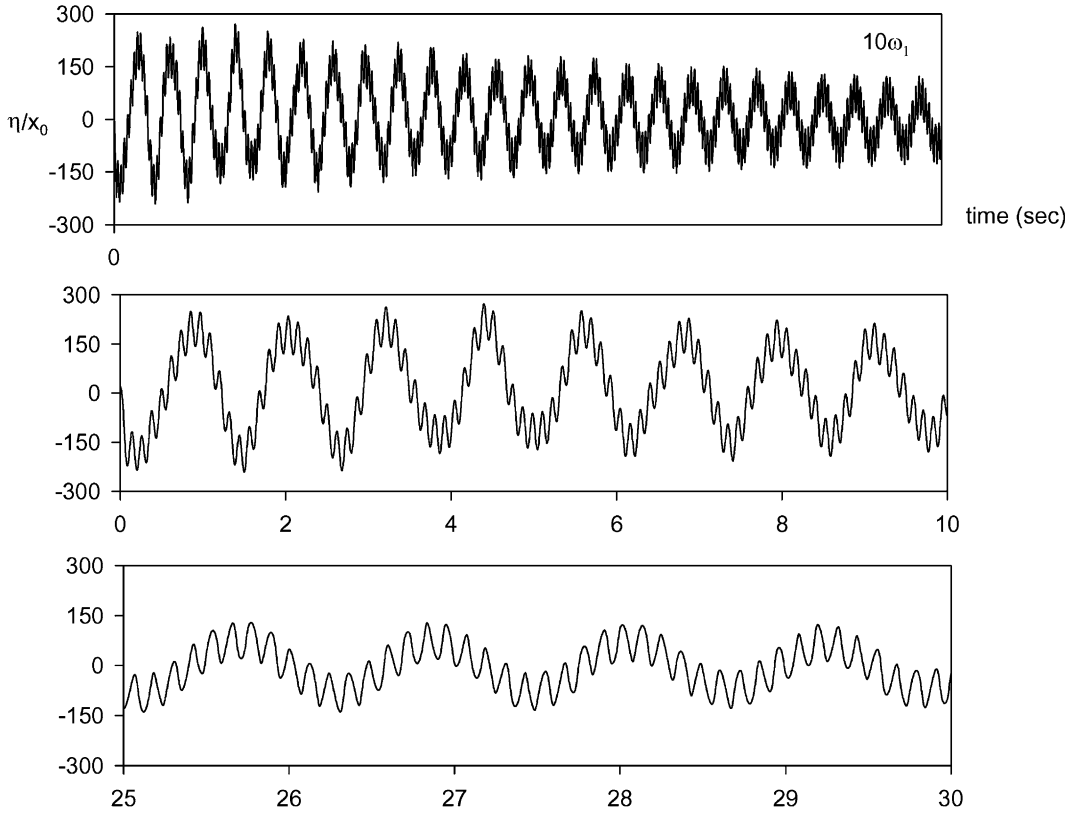

Fig. 22. Under surge motion, the time-history of surface displacement at left tank wall with exciting frequency = $10\omega_1$.

Table 1
The ratio of the sloshing displacements

Case	1	2	3	4	5	6	7	8	9
x_0 (m)	0.005	0.007	0.01	0.005	0.007	0.01	0.005	0.007	0.01
ω_x (rad/s)	5	5	5	5	5	5	5	5	5
B (m)	1	1	1	1	1	1	1	1	1
d_0 (m)	0.1	0.1	0.1	0.15	0.15	0.15	0.2	0.2	0.2
η^+/η^-	1.38	1.71	2.15	2.0	2.10	2.42	2.12	2.77	2.9
	10	11	12	13	14	15	16	17	
x_0 (m)	0.005	0.007	0.005	0.007	0.005	0.007	0.005	0.007	
ω_x	$0.95\omega_1$	$0.95\omega_1$	$0.95\omega_1$	$0.95\omega_1$	$0.95\omega_1$	$0.95\omega_1$	$0.95\omega_1$	$0.95\omega_1$	
B (m)	1	1	1	1	1	1	1	1	
d_0 (m)	0.1	0.1	0.15	0.15	0.2	0.2	0.5	0.5	
η^+/η^-	1.55	1.8	1.9	2.25	1.9	2.54	1.2	1.3	

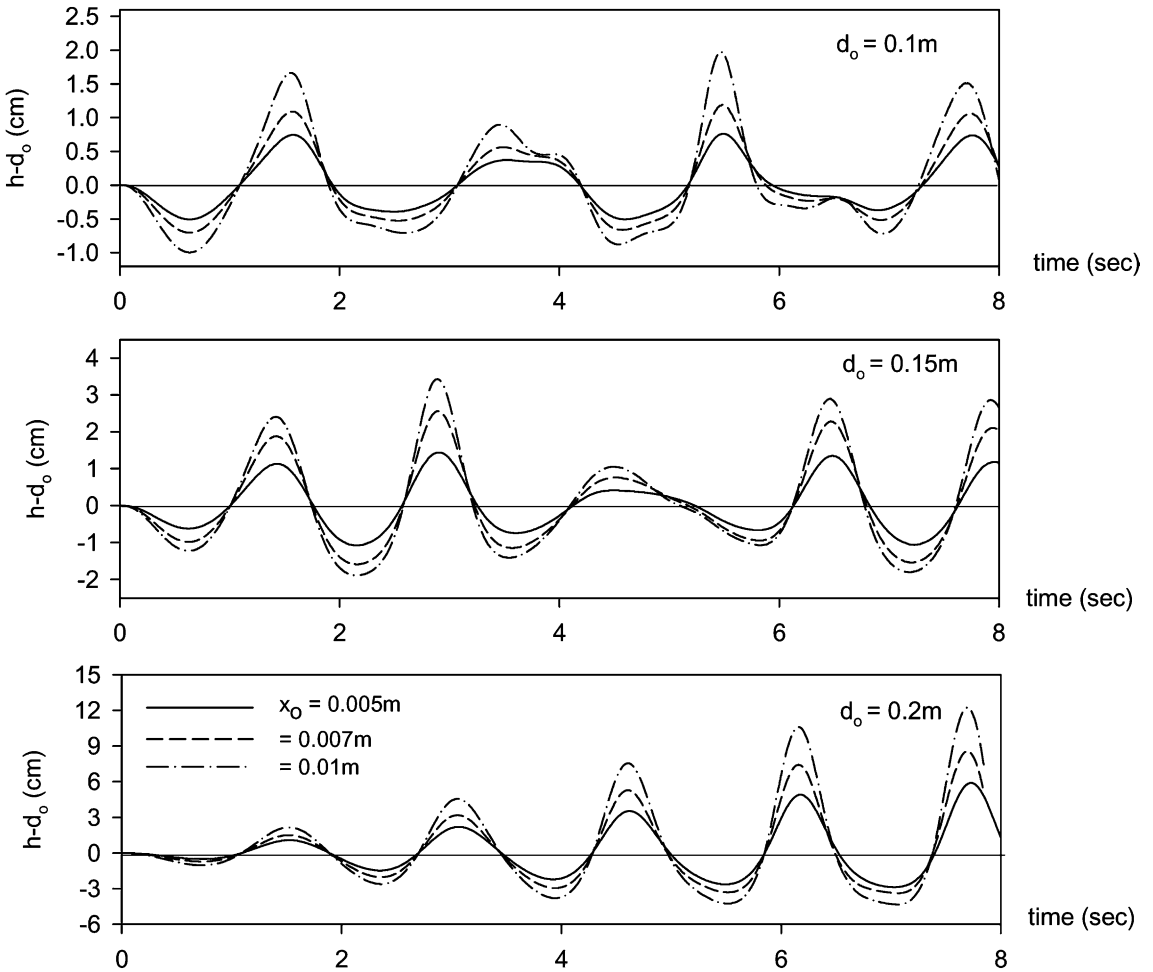

Fig. 23. The sloshing displacements at left wall under surge motion with constant surge frequency $\omega_x = 5$ rads/s, constant tank width = 1 m and various water depths and various exciting surge displacement.

frequency, together with the excitation frequency, dominate the frequency of the system during the initial time period. However, by $t = 40$–50 s, the significance of the fundamental frequency is significantly reduced and the frequency of excitation becomes dominant. The reason for this is that the periods of the excitation for $\omega_x = 1.5\omega_1$–$2\omega_1$ are smaller than that for $\omega_x < \omega_1$, and the system needs more time to adjust to the pace of the external excitation. The excitation frequency will control the system at the later period as the system responds to the external forcing and the influence of ω_1 diminishes.

When the frequency of excitation is larger than $3\omega_1$ (see Fig. 22), the period of the external excitation is too short to let the dynamic system adjust to the frequency of the excitation and the first fundamental frequency, therefore, becomes the dominant frequency of the system throughout the entire time history.

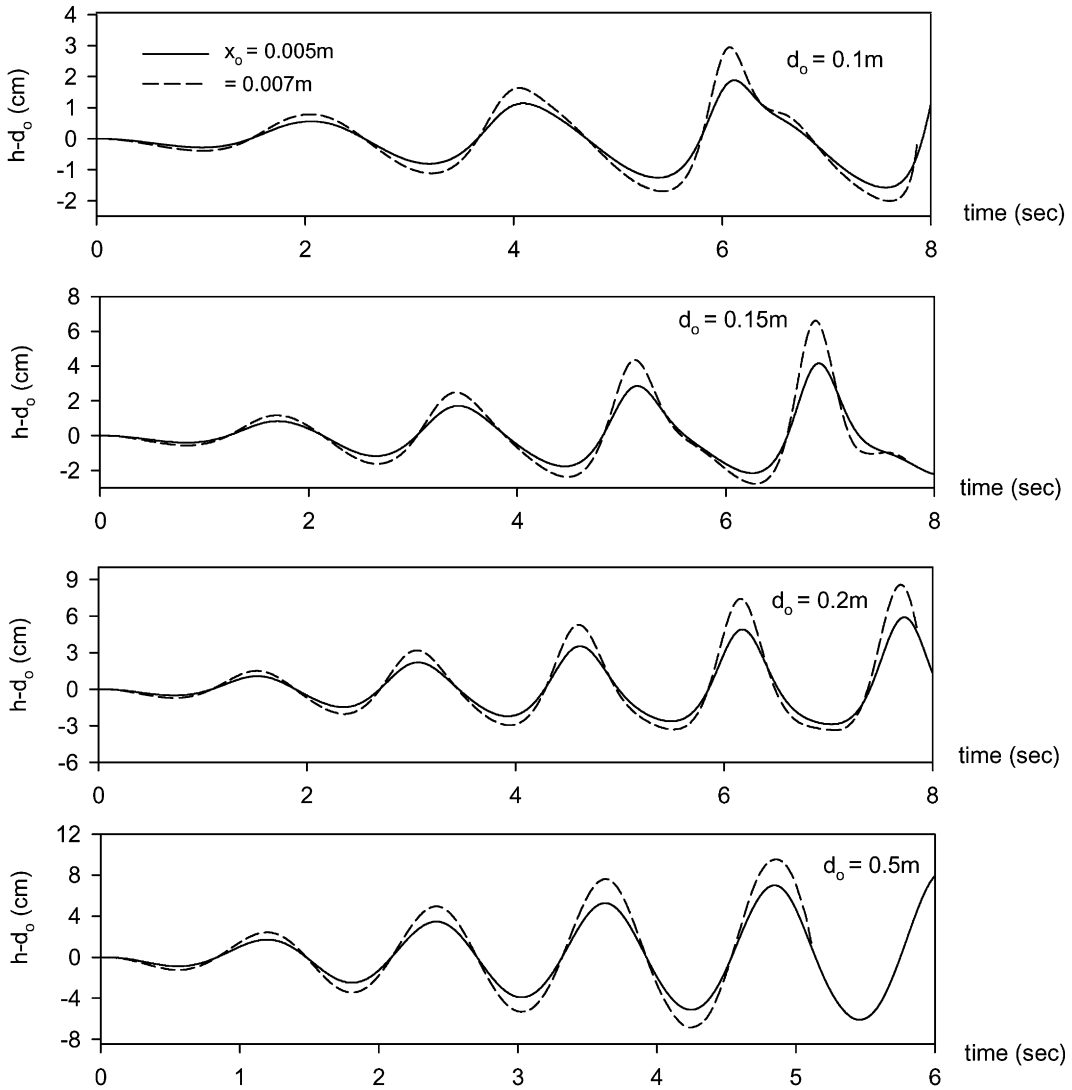

Fig. 24. The sloshing displacement under near resonant excitation with various exciting surge displacement and water depths, $\omega_x = 0.95\ \omega_1$.

In this case, the effect of the excitation frequency on the sloshing displacement seems to be at the level of noise.

5.7. The limitation of the proposed scheme

In this section, extensive simulations were made to test the limitation of the present time-independent finite-difference scheme. Table 1 shows the cases that were simulated in this section. For each depth/width ratio (d_0/B), four excitation displacements were applied: $x_0 = 0.005$, 0.007, 0.01 and 0.015 m. Each simulation lasted for 8 s. The simulations for $x_0 = 0.015$ m were all divergent before $t = 5$ s and those results are not included in the table for comparison. Two excitation frequencies were used in the simulations, one was $\omega_x = 5$ rads/s $= 0.87\omega_1$, the other was $\omega_x = 0.95\omega_1$ so that near resonant simulations could be performed.

The corresponding sloshing histories of $\omega_x = 5$ rad/s and $\omega_x = 0.95\omega_1$ are shown in Figs. 23 and 24, respectively. The parameter η^+ represents the sloshing peak and η^- represents the trough. For $\omega_x = 5$ rad/s, the non-linear characteristics of the problem are clearly visible for small d_0/B ratio. Increases in sloshing displacement occur as the excitation amplitude increases. For $x_0 = 0.01$ m and $d_0/B = 0.1$, the largest η^+/η^- ratio can be as large as 2.15 and this increases with increasing d_0/B, with η^+/η^- ratios of 2.42 and 2.9 for $d_0/B = 0.15$ and $d_0/B = 0.2$, respectively. The simulation for $d_0/B = 0.05$ are divergent and the results are not listed in the table for comparison.

For near resonant oscillation, $\omega_x = 0.95\omega_1$, the simulations for $x_0 = 0.01$ m are divergent for all cases. For $x_0 = 0.005$ m and $x_0 = 0.007$ m, the η^+/η^- ratios are about the same as those for $\omega_x = 5$ rad/s for $d_0/B = 0.1$ and $d_0/B = 0.15$, and the η^+/η^- ratio is smaller than that for $\omega_x = 5$ rad/s and $d_0/B = 0.2$. The η^+/η^- ratio reduces to around 1 for $d_0/B = 0.5$. The proposed scheme can be applied in a non-resonant oscillation with x_0 up to 0.01 m. But the depth/breadth ratio (d_0/B) is limited to 0.1 in all simulations.

6. Conclusions

A new time-independent finite difference method has been developed and used to study coupled two-dimensional and fully non-linear, viscous sloshing motion in tanks. The following conclusions can be drawn:

1. The time-dependent domain is transformed to a fixed unit square by proper mapping functions. In this method, re-meshing due to a wavy free surface is avoided and free surface smoothing is also not required. The meshes near the boundary are stretched to capture the local sharp variations due to viscosity. The finite difference expressions for the viscous diffusion terms are applied in the proper location to overcome the difficulties associated with decreasing meshes and loss of accuracy.
2. The maximum transient amplitude is much larger than that of the steady-state response. Clear beating phenomenon occurs when the tank is excited by a near resonance frequency. The viscous effects shift the resonance frequency peak and also retard the beating phenomenon.
3. For a given frequency, the sloshing amplitude of the free surface at the wall increases linearly with Reynolds number. In other words, for a fixed excitation frequency, the displacement of the sloshing surface is linearly proportional to the horizontal displacement due to the excitation. However, for a constant Reynolds number, the sloshing displacement is frequency dependent.
4. Vertical excitation changes the acceleration due to gravity as well as the Froude number of the system, and this can significantly affect the sloshing displacement. The coupled effects of simultaneous surge, heave and pitch motions are observed as the non-linearity of the problem becomes prominent, and it is clear that the coupled motion should be included in the sloshing analysis when the tank is excited by earthquakes.

5. The formation of an eddy occurs during the transient period of tank motion under pitch forcing. This eddy reduces the surface elevation in the tank and enhances mixing of the fluid in the tank. A particular combination of coupled surge and pitch motion increases the lifetime of the eddy and hence would achieve better fluid mixing.
6. A simple formula is derived to evaluate the horizontal forces acting on the tank wall. The force is controlled by the added mass effect when the frequency of excitation is large. In contrast, for small excitation frequencies, the force is proportional to the sloshing displacement at the wall.
7. An FFT analysis of sloshing displacement shows that the dynamic system is controlled by the forcing frequency when the period of the excitation is large enough for the system to adjust to the external excitation. For a very large forcing frequency, the fundamental frequency will completely dominate the sloshing fluid.
8. The present numerical method is found to converge for non-resonant oscillation frequencies with a maximum surge amplitude up to $0.02d_0$ and a depth/breadth ratio larger than 0.1.

The time-independent finite difference method introduced in this paper can be extended to the analysis of three-dimensional tank motions excited simultaneously by six-degree of freedom of motions (surge, pitch, heave, yaw, roll and sway).

Acknowledgments

The authors thank the valued comments offered by the reviewers and the associate editor. The study is partially supported by the NSC of ROC under Grant No. NSC-93-2611-E110-006. Part of the study is made during the author visiting at the Department of Civil Engineering, University of Canterbury. The author thanks H.-W. Chiang and T.-H. Wu for helping computer coding and plotting figures.

Appendix I

The coefficients C_1–C_{10} are:

$$C_1 = d_0\frac{\partial x^*}{\partial x} = \frac{d_0}{b_2 - b_1},$$

$$C_2 = d_0\frac{\partial z^*}{\partial x} = \frac{1}{H^2}(z + d_0)\frac{\partial H}{\partial x},$$

$$C_3 = -d_0\frac{\partial x^*}{\partial z} = -\frac{d_0}{(b_2 - b_1)^2}\left[(x - b_2)\frac{\partial b_1}{\partial z} - (x - b_1)\frac{\partial b_2}{\partial z}\right],$$

$$C_4 = -d_0\frac{\partial z^*}{\partial z} = \frac{1}{H},$$

$$C_5 = \frac{d_0}{\sqrt{gd_0}}\frac{\partial x^*}{\partial t} = -\frac{d_0}{\sqrt{gd_0}(b_2 - b_1)^2}\left[(x - b_2)\frac{\partial b_1}{\partial t} - (x - b_1)\frac{\partial b_2}{\partial t}\right],$$

$$C_6 = \frac{d_0}{\sqrt{gd_0}}\frac{\partial z^*}{\partial t} = \frac{1}{\sqrt{gd_0}H^2}(z + d_0)\frac{\partial H}{\partial x},$$

$$C_7 = \frac{\partial X}{\partial x^*} = [1 + k_1(x^* - \beta_1)(2x^*) - 1]\mathrm{e}^{k_1 x^*(x^*-1)},$$

$$C_8 = \frac{\partial Z}{\partial z^*} = [1 + k_2(z^* - \beta_2)(2z^*) - 1]\mathrm{e}^{k_{21} z^*(z^*-1)},$$

$$C_9 = 4\pi^2 \frac{x}{d_0},$$

$$C_{10} = 2\pi \frac{z}{d_0},$$

$$\lambda = \frac{d_0}{B}.$$

Appendix II

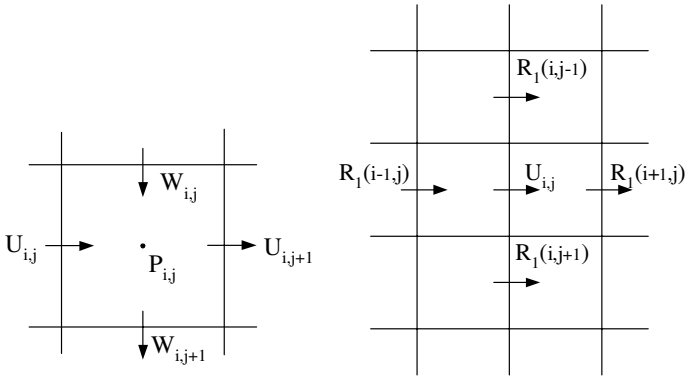

$$R_1 = C_1 C_7 \frac{\partial U}{\partial X} + C_2 C_8 \frac{\partial U}{\partial Z},$$

$$\frac{1}{Re}\left(C_1 C_2 \frac{\partial R_1}{\partial X} + C_2 C_8 \frac{\partial R_1}{\partial Z}\right)_{\text{at } U_{i,j}} = \frac{1}{R_e}\left[(C_1 C_2)_{U_{i,j}} \frac{R_1(i+1,j) - R_1(i-1,j)}{2\Delta X} + (C_2 C_8)_{U_{i,j}} \frac{R_1(i,j+1) - R_1(i,j-1)}{2\Delta Z}\right],$$

where:

$$R_1(i+1,j) = (C_1 C_7)_{U_{i+1,j}} \frac{U_{i+2,j} - U_{i,j}}{2\Delta X} + (C_2 C_8)_{U_{i+1,j}} \frac{U_{i+1,j+1} - U_{i+1,j-1}}{2\Delta Z},$$

$$R_1(i-1,j) = (C_1 C_7)_{U_{i-1,j}} \frac{U_{i,j} - U_{i-2,j}}{2\Delta X} + (C_2 C_8)_{U_{i-1,j}} \frac{U_{i-1,j+1} - U_{i-1,j-1}}{2\Delta Z},$$

$$R_1(i,j+1) = (C_1 C_7)_{U_{i,j+1}} \frac{U_{i+1,j+1} - U_{i-1,j+1}}{2\Delta X} + (C_2 C_8)_{U_{i,j+1}} \frac{U_{i,j+2} - U_{i,j}}{2\Delta Z},$$

$$R_1(i,j-1) = (C_1C_7)_{U_{i,j-1}} \frac{U_{i+1,j-1} - U_{i-1,j+1}}{2\Delta X} + (C_2C_8)_{U_{i,j-1}} \frac{U_{i,j} - U_{i,j-2}}{2\Delta Z}.$$

Note that, $(C_1C_7)_{U_{i,j-1}}$ denotes (C_1C_7) are evaluated at $U_{i,j-1}$ position, the other terms have similar meanings.

Appendix III

Consider the finite difference solution to the one-dimensional diffusion equation

$$\partial u/\partial t = \alpha \partial^2 u/\partial x^2 \tag{AIII-1}$$

with the following boundary conditions: $u(0,t) = 0$, $u(0.04,t) = 40$ m/s. A domain mesh that is stretched by $X = \beta_1 + (x - \beta_1)e^{k_1 x(x-1)}$, with $\beta_1 = 1.0$ and $k_1 = 1.0$, with $\Delta X = 1/40$ is illustrated in Fig. AIII-I in the original x coordinate system. After the coordinate transformation (stretching), Eq. (AIII-1) is transformed into

$$\partial u/\partial t = \alpha C^2 \partial^2 u/\partial X^2,$$

where $C = \partial X/\partial x$. The accuracies of three different finite difference approximations, given in Eqs. (AIII-2) and (AIII-4), are compared:

$$u_i^{n+1} = u_i^n + \Delta t/\Delta X^2 C_i^2 \left(u_{i+1}^{n+1/2} - 2u_i^{n+1/2} + u_{i-1}^{n+1/2}\right), \tag{AIII-2}$$

$$u_i^{n+1} = u_i^n + \Delta t/\Delta X C_i \left\{ C_{i+1/2}\left(u_{i+1}^{n+1/2} - u_i^{n+1/2}\right) - C_{i-1/2}\left(u_i^{n+1/2} - u_{i-1}^{n+1/2}\right) \right\} \Big/ \Delta X, \tag{AIII-3}$$

$$u_i^{n+1} = u_i^n + \Delta t/\Delta X C_i \{ C_{i+1/2}\left(u_{i+1}^n - u_i^n\right) - C_{i-1/2}\left(u_i^n - u_{i-1}^n\right) \}/\Delta X, \tag{AIII-4}$$

where C_i is C at u_i position, $C_{i+1/2}$ and $C_{i-1/2}$ are C at $u_{i+1/2}$ and $u_{i-1/2}$ positions, respectively. The superscripts of u denotes the time steps, i.e., u_i^{n+1} represents u_i at $T = (n+1)\Delta T$, the other terms have similar meaning. Eqs. (AIII-2) and (AIII-3) use the Crank–Nicolson (C–N) method, while Eq. (AIII-4) uses the forward time central space (FTCS) method.

Fig. AIII-II compares the results obtained using Eqs. (AIII-2)–(AIII-4) with the exact solution. As can be seen in the figure, the results obtained using Eq. (AIII-3) are the best. Large errors are created when Eq. (AIII-2) is used. The results shown in Fig. AIII-II justify the adoption of the finite difference approximation listed in Appendix II for the solution of Eqs. (12) and (13).

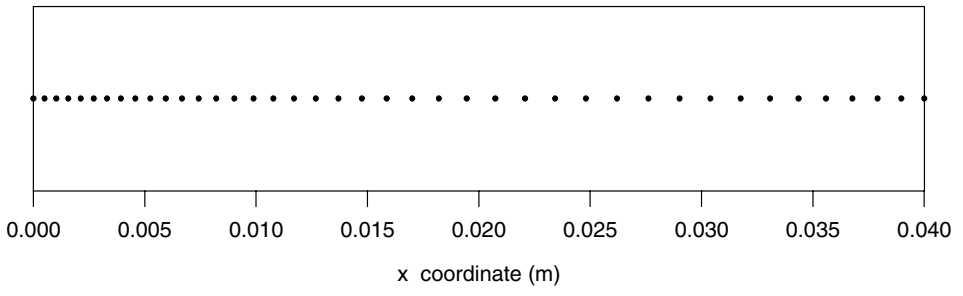

Fig. AIII-I. The coordinate of each node in x-system after coordinate stretching.

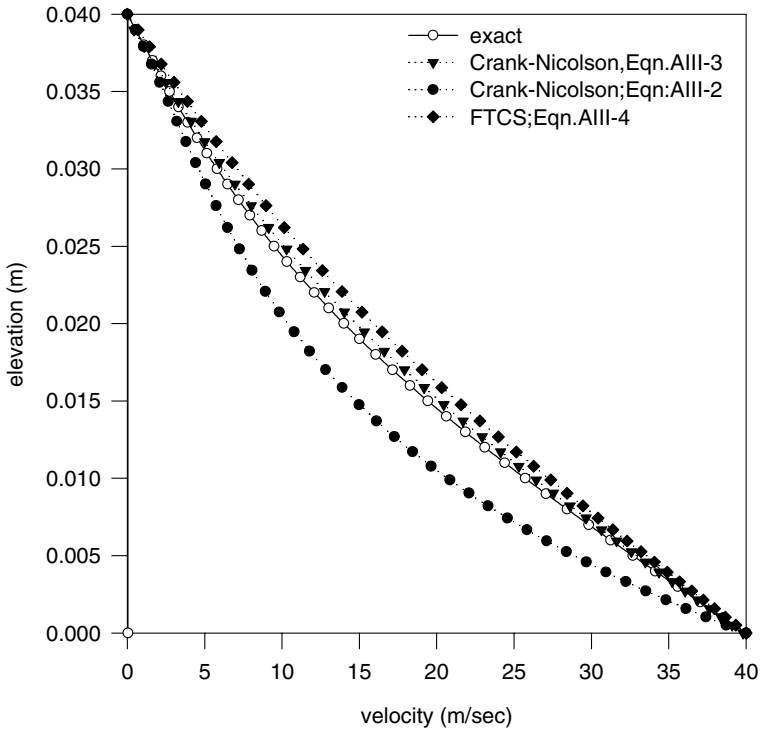

Fig. AIII-II. The comparison of solution of the accelerated lower plate by the Crank–Nicolson Scheme (Eq. (AIII-2)), Crank–Nicolson Scheme (Eq. (AIII-3)) and FTCS (Eq. (AIII-4)).

References

[1] V. Armenio, M.L. Rocca, On the analysis of sloshing of water in rectangular containers: numerical study and experimental validation, Ocean Eng. 23 (8) (1996) 705–739.
[2] D.C. Barton, J.V. Parker, Finite element analysis of the seismic response of anchored and unanchored liquid storage tanks, Earthquake Eng. Struct. Dyn. 15 (1987) 299–322.
[3] J. Billinghen, Nonlinear sloshing in zero gravity, J. Fluid Mech. 464 (2002) 365–391.
[4] A. Cariou, G. Casella, Liquid sloshing in ship tanks: a comparative study of numerical simulation, Marine Struct. 12 (1999) 183–198.
[5] M.S. Celebi, H. Akyildiz, Nonlinear modeling of liquid sloshing in a moving rectangular tank, Ocean Eng. 29 (2002) 1527–1553.
[6] B.F. Chen, Viscous free surface effects on coastal embankment hydrodynamics, Ocean Eng. 26 (1999) 47–65.
[7] B.F. Chen, S.W. Chiang, Complete 2D and fully nonlinear analysis of sloshing fluid in a rigid; ideal fluid, J. Eng. Mech. 125 (1) (1999) 70–78.
[8] R.G. Cox, The dynamics of spreading of liquids on a solid surface. Part I. Viscous floe, J. Fluid Mech. 168 (1986) 169–194.
[9] O.M. Faltinsen, A numerical non-linear method of sloshing in tanks with two dimensional flow, J. Ship Res. 31 (2) (1978) 125–135.
[10] J.B. Frandsen, Sloshing motions in excited tanks, J. Comput. Phys. 196 (2004) 53–87.
[11] D.F. Hill, Transient and steady-state amplitudes of forced waves in rectangular basins, Phys. Fluids 15 (6) (2003) 1576–1587.
[12] C.J. Huang, E.C. Zhang, J.F. Lee, Numerical simulation of nonlinear viscous wavefields generated by a piston-type wavemaker, J. Eng. Mech. 124 (1998) 1110–1120.
[13] Y. Kim, Numerical simulation of sloshing flows with impact loads, Appl. Ocean Res. 23 (2001) 53–62.
[14] C.G. Koh, S. Mahatma, C.M. Wang, Theoretical and experimental studies on rectangular liquid dampers under arbitrary excitations, Earthquake Eng. Str. Dynam. 23 (1994) 17–31.
[15] G.L. Meller, A.F. Blumberg, Modelling vertical and horizontal diffusivities with the sigma transform system, Appl. Ocean Res. 113 (1985) 1379–1383.

[16] T. Nakayama, K. Washizu, The boundary element method applied to the analysis of two-dimensional nonlinear sloshing problems, Int. J. Numer. Meth. Eng. 17 (1981) 1631–1646.
[17] N.A. Phillps, A coordinate system having some special advantages for numerical forecasting, J. Meteorol. 14 (1957) 184–185.
[18] C.J. Tang, V.C. Patel, L. Landweber, Viscous effects on propagation and reflection of solitary waves in shallow channels, J. Comput. Phys. 88 (1) (1990) 86–114.
[19] A.S. Veletsos, P. Shivakumar, Dynamic response of rigid tanks with inhomogeneous liquids, Earthquake Eng. Struct. Dyn. 24 (1995) 991–1015.
[20] G.X. Wu, Q.W. Ma, R. Eatock Taylor, Numerical simulation of sloshing waves in a 3D tank based on a finite element methods, Appl. Ocean Res. 20 (1998) 337–355.
[21] G.X. Wu, R. Eatock Taylor, D.M. Greaves, The effect of viscosity on the transient free-surface waves in a two-dimensional tank, J. Eng. Math. 40 (2001) 77–90.
[22] T.K. Hung, B.F. Chen, Nonlinear hydrodynamic pressure on dams during earthquake, J. Eng. Mech. ASCE 116 (6) (1990) 1372–1391.
[23] A.T. Chwang, G.W. Housner, Hydrodynamic pressures on sloping dams during earthquakes: part I, momentum method, J. Fluid Mech. 67 (1978) 335–341.
[24] E. Dussan, The moving contact line: the slip boundary condition, J. Fluid Mech. 77 (4) (1976) 665–684.
[25] E.B. Dussan, On the spreading of liquids on solid surfaces: static and dynamic contact lines, Ann. Rev. Fluid Mech. 11 (1979) 371.
[26] L.M. Hocking, The damping of capillary-gravity waves at a rigid boundary, J. Fluid Mech. 179 (1987) 253–266.
[27] T.C. Huang, Engineering Mechanics, vol. II, Dynamics, Addison-Wesley Publishing Company Inc., New York, 1967.
[28] R.A. Ibrahim, V.N. Pilipchuk, T. Ikeda, Recent advances in liquid sloshing dynamics, Appl. Mech. Res. 54 (2) (2001) 133–199.
[29] T. Okamoto, M. Kawahara, Two-dimensional sloshing analysis by Lagragian finite element method, Int. J. Numer. Meth. Fluid 11 (1990) 453–477.
[30] T. von Kármán, in: H.M. Westergarrd (Ed.), Discussion of the Water Pressures on Dam during Earthquakes, Trans. ASCE, vol. 98, 1933, pp. 434–436.